

# Water deuterium fractionation in the high-mass star-forming region G34.26+0.15 based on *Herschel*/HIFI data

A. Coutens<sup>1,2\*</sup>, C. Vastel<sup>3,4</sup>, U. Hincelin<sup>5</sup>, E. Herbst<sup>5</sup>, D. C. Lis<sup>6,7</sup>, L. Chavarría<sup>8</sup>,  
M. Gérin<sup>9</sup>, F. F. S. van der Tak<sup>10,11</sup>, C. M. Persson<sup>12</sup>, P. F. Goldsmith<sup>13</sup>, E. Caux<sup>3,4</sup>

<sup>1</sup> Niels Bohr Institute, University of Copenhagen, Juliane Maries Vej 30, DK-2100 Copenhagen Ø, Denmark

<sup>2</sup> Centre for Star and Planet Formation, Natural History Museum of Denmark, University of Copenhagen, Øster Voldgade 5-7, DK-1350 Copenhagen K, Denmark

<sup>3</sup> Université de Toulouse, UPS-OMP, IRAP, Toulouse, France

<sup>4</sup> CNRS, Institut de Recherche en Astrophysique et Planétologie, 9 Av. Colonel Roche, BP 44346, 31028 Toulouse Cedex 4, France

<sup>5</sup> Department of Chemistry, University of Virginia, McCormick Road, Charlottesville, VA 22904, USA

<sup>6</sup> California Institute of Technology, Cahill Center for Astronomy and Astrophysics 301-17, Pasadena, CA 91125, USA

<sup>7</sup> Sorbonne Universités, Université Pierre et Marie Curie, Paris 6, CNRS, Observatoire de Paris, UMR 8112, LERMA, Paris, France

<sup>8</sup> Universidad de Chile - CONICYT, Camino del Observatorio 1515, Las Condes, Santiago

<sup>9</sup> LERMA-LRA, UMR 8112 du CNRS, Observatoire de Paris, Ecole Normale Supérieure, UPMC & UCP, 24 rue Lhomond, 75231 Paris Cedex 05, France

<sup>10</sup> SRON Netherlands Institute for Space Research, Landleven 12, 9747 AD Groningen, The Netherlands

<sup>11</sup> Kapteyn Astronomical Institute, University of Groningen, 9700 AV Groningen, The Netherlands

<sup>12</sup> Chalmers University of Technology, Department of Earth and Space Sciences, Onsala Space Observatory, 43992 Onsala, Sweden

<sup>13</sup> Jet Propulsion Laboratory, California Institute of Technology, Pasadena, CA 91125, USA

Accepted xxx. Received xxx; in original form xxx

## ABSTRACT

Understanding water deuterium fractionation is important for constraining the mechanisms of water formation in interstellar clouds. Observations of HDO and H<sub>2</sub><sup>18</sup>O transitions were carried out towards the high-mass star-forming region G34.26+0.15 with the HIFI instrument onboard the *Herschel* Space Observatory, as well as with ground-based single-dish telescopes. Ten HDO lines and three H<sub>2</sub><sup>18</sup>O lines covering a broad range of upper energy levels (22–204 K) were detected. We used a non-LTE 1D analysis to determine the HDO/H<sub>2</sub>O ratio as a function of radius in the envelope. Models with different water abundance distributions were considered in order to reproduce the observed line profiles. The HDO/H<sub>2</sub>O ratio is found to be lower in the hot core ( $\sim 3.5 \times 10^{-4}$ – $7.5 \times 10^{-4}$ ) than in the colder envelope ( $\sim 1.0 \times 10^{-3}$ – $2.2 \times 10^{-3}$ ). This is the first time that a radial variation of the HDO/H<sub>2</sub>O ratio has been found to occur in a high-mass source. The chemical evolution of this source was modeled as a function of its radius and the observations are relatively well reproduced. The comparison between the chemical model and the observations leads to an age of  $\sim 10^5$  years after the infrared dark cloud stage.

**Key words:** astrochemistry – ISM: individual object: G34.26+0.15 – ISM: molecules – ISM: abundances

## 1 INTRODUCTION

Water, being necessary for the emergence of life, is one of the most important molecules found in space. As a dominant form of oxygen (the most abundant element in the Universe after hydrogen and helium), water controls the chemistry of many other species, whether in the gas phase or in the solid phase (see for example the review by van Dishoeck et al. 2013). Water is a unique diagnostic of the warmer gas and the energetic processes taking place close to star-forming regions. Water is also a contributor to maintaining the low

temperature of the gas by spectral line radiative cooling. Low temperatures are a requisite for cloud collapse and star formation. Water is mainly in its solid form (as ice on the surface of dust grains) in the cold regions of the interstellar medium as well as in asteroids and comets that likely delivered water to the Earth's oceans (e.g., Hartogh et al. 2011; Alexander et al. 2012). Therefore, constraining the distribution of water vapor and ice during the entire star and planet formation phase is mandatory to understand our own origins.

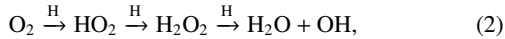
Because of its high abundance in our own atmosphere, observations of interstellar water have been primarily carried out from space observatories including ISO, *Spitzer*, ODIN, SWAS, and recently *Herschel*. Indeed, water has been detected toward the cold prestellar core L1544 (Caselli et al. 2012), many low-mass proto-

\* E-mail: acoutens@nbi.dk

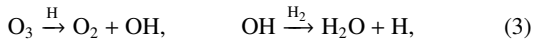
stars (e.g., Coutens et al. 2012; Kristensen et al. 2010, 2012), high-mass protostars (e.g., van der Tak et al. 2013; Emprechtinger et al. 2013), in the disk of a young star TW Hydrae (Hogerheijde et al. 2011), as well as in many comets (e.g., 103P/Hartley 2: Hartogh et al. 2011, C/2009 P1 (Garradd): Bockelée-Morvan et al. 2012, 45P/Honda-Mrkos-Pajdušáková: Lis et al. 2013) and in asteroids (24 Themis: Campins et al. 2010, Ceres: Küppers et al. 2014). The water abundance shows a very large variation from one source category to another, as well as within each type of sources. The question then arises: how is water produced and why are its abundance variations so large? Although production in the gas phase followed by direct condensation onto dust grains is possible (Bergin et al. 1999), observations favor formation through chemical reactions on the surface of cold dust grains. Indeed, in comparison to gas-phase water abundance, the observed water ice abundance is too high to be entirely explained by direct accretion from the gas-phase (Roberts & Herbst 2002). Consequently surface reactions on cold dust grains to form water molecules have been investigated with modern surface science techniques (e.g. Watanabe & Kouchi 2008). Considering the large reservoir of oxygen and hydrogen atoms in molecular clouds, large amounts of water ice might be produced (Dulieu et al. 2010) following the successive hydrogenation of oxygen on grain surfaces:



Tielens & Hagen (1982) proposed that water ice might also be produced through the successive hydrogenation of molecular oxygen:



demonstrated by Miyauchi et al. (2008), Ioppolo et al. (2008) and Oba et al. (2009), or by hydrogenation of ozone:



demonstrated by Mokrane et al. (2009).

Deuterated water is likely to be formed through the same processes. Many rotational transitions have been detected from the ground, as well as with *Herschel*/HIFI, for example in low-mass protostars (Parise et al. 2005; Liu et al. 2011; Coutens et al. 2012, 2013; Persson et al. 2013, 2014), high-mass star forming regions (e.g., Jacq et al. 1990; Gensheimer et al. 1996), and comets (e.g., Bockelée-Morvan et al. 1998; Hartogh et al. 2011; Lis et al. 2013). The HDO/H<sub>2</sub>O ratio is an interesting diagnostic tool to help understand the origin of water in the interstellar medium, with a direct comparison with the D/H ratio observed in comets and in the Earth's oceans. It is also helpful to constrain the water formation conditions. In star-forming regions, observations of both high- and low-excitation water lines with a high spectral resolution are needed to disentangle the contributions from the hot cores (or hot corinos in the case of low-mass protostars) and the colder external envelope, that can be linked to the parental cloud, in which stars form. Near protostars, the grain temperature rises above ~100 K, leading to rapid water ice desorption that increases the gas-phase H<sub>2</sub>O (and its deuterated counterparts) abundance in the inner parts of the envelope. In order to interpret the observed spectra in terms of local physical conditions and relative abundances, radiative transfer modeling is necessary. This is illustrated with the modeling performed by Coutens et al. (2012, 2013) toward the low-mass protostar IRAS 16293-2422, where numerous HDO, H<sub>2</sub><sup>18</sup>O, and D<sub>2</sub>O transitions have been used simultaneously to constrain the abundances in the hot corino, in the cold envelope, and in a water-rich absorbing layer surrounding the envelope.

This paper reports full statistical equilibrium and radiative transfer calculations towards the ultra compact HII region G34.26+0.15 (hereafter G34) using both ground-based observations and *Herschel*/HIFI observations of HDO and the less abundant H<sub>2</sub><sup>18</sup>O water isotopologue. The paper is organized as follows. In Sections 2 and 3, we describe the source and the observations respectively. In Section 4, we present results obtained both with a simple local thermal equilibrium modeling (LTE) and with the 1D non-LTE modeling. In Section 5, we compare them with a chemical model. Finally, we present our conclusions in Section 6.

## 2 SOURCE DESCRIPTION

Located at a distance of ~3.3 kpc (Kuchar & Bania 1994), G34 has been widely studied in radio continuum (Turner et al. 1974; Reid & Ho 1985; Wood & Churchwell 1989; Sewilo et al. 2011) and radio recombination lines (Garay et al. 1985, 1986; Gaume et al. 1994; Sewilo et al. 2004, 2011). Several components have been identified in radio continuum observations: two ultra compact HII regions called A and B, a more evolved HII region with a cometary shape (component C), and an extended (1') HII region (component D) in the south-east. Chemical surveys were carried out towards the A, B and C components using single-dish telescopes (MacDonald et al. 1996; Hatchell et al. 1998) and interferometric observations (Mookerjee et al. 2007). Many complex species, characteristic of hot cores, have been detected. From molecular line observations, the emission peak does not coincide with the HII components (Watt & Mundy 1999; De Buizer et al. 2003), but is shifted to the East of the component C by ~1'' (Mookerjee et al. 2007: Figure 3). This difference may arise due to the external influence of the nearby HII regions, or may reveal separate regions of chemical enrichment. The hot core is likely externally heated by stellar photons rather than by shocks, as SiO was not detected at the position of the hot core (Hatchell et al. 2001). This source is also characterized by infall motions as suggested by observations of absorption components of NH<sub>3</sub>, CN, HCN and HCO<sup>+</sup> (Wyrowski et al. 2012; Liu et al. 2013, Hajigholi et al. in prep.).

The hot core of G34 has been the target of many *Herschel*/HIFI observations for the past four years, including water line emission (Flagey et al. 2013) and its deuterated counterparts. We present in Section 3 the H<sub>2</sub><sup>18</sup>O and HDO transitions observed from the ground as well as the *Herschel*/HIFI observations. Note that the Half-Power Beam Width (HPBW) of those telescopes encompasses the components A and B and the molecular peak from component C for all observations.

## 3 OBSERVATIONS

### 3.1 Observations and data reduction

This source is part of the PRISMAS Key Program (PRobing Inter-Stellar Molecules with Absorption line Studies; Gerin et al. 2010) which was followed by an Open Time Program led by C. Vastel. The targeted coordinates are  $\alpha(\text{J2000}) = 18^{\text{h}}53^{\text{m}}18.7^{\text{s}}$ ,  $\delta(\text{J2000}) = 01^{\circ}14'58''$ . The observations were performed in the pointed dual beam switch (DBS) mode using the double sideband (DSB) HIFI instrument (de Graauw et al. 2010; Roelfsema et al. 2012) onboard the *Herschel* Space Observatory (Pilbratt et al. 2010). The DBS reference positions were situated approximately 3' east and west of the source. The HIFI Wide Band Spectrometer (WBS) was used

**Table 1.** HDO and H<sub>2</sub><sup>18</sup>O transitions observed towards the ultra-compact HII region G34<sup>(1)</sup>.

Species	Frequency (GHz)	$J_{K_a,K_c}$	$E_{up}/k$ (K)	$A_{ij}$ (s <sup>-1</sup> )	Telescope	HPBW ( $''$ )	$F_{eff}$	$B_{eff}$	$dv$ (km s <sup>-1</sup> )	$rms^{(2)}$ (mK)	$\int T_{mb} dv$ (K km s <sup>-1</sup> )	$FWHM$ (km s <sup>-1</sup> )
HDO	80.5783	1 <sub>1,0</sub> –1 <sub>1,1</sub>	47	$1.32 \times 10^{-6}$	IRAM-30m	31.2	0.95	0.81	0.182	56	2.36	5.9
	225.8967	3 <sub>1,2</sub> –2 <sub>2,1</sub>	168	$1.32 \times 10^{-5}$	IRAM-30m	11.1	0.92	0.61	0.064	101	10.45	6.7
	241.5616	2 <sub>1,1</sub> –2 <sub>1,2</sub>	95	$1.19 \times 10^{-5}$	IRAM-30m	10.4	0.90	0.56	0.061	84	12.27	6.6
	464.9245	1 <sub>0,1</sub> –0 <sub>0,0</sub>	22	$1.69 \times 10^{-4}$	CSO	16.5	-	0.35 <sup>(3)</sup>	0.078	304	7.48	5.2
	490.5966	2 <sub>0,2</sub> –1 <sub>1,1</sub>	66	$5.25 \times 10^{-4}$	HIFI 1a	43.9	0.96	0.76	0.305	10	2.13	7.6
	509.2924	1 <sub>1,0</sub> –1 <sub>0,1</sub>	47	$2.32 \times 10^{-3}$	HIFI 1a	42.3	0.96	0.76	0.294	44	1.76	9.0
	599.9267	2 <sub>1,1</sub> –2 <sub>0,2</sub>	95	$3.45 \times 10^{-3}$	HIFI 1b	35.9	0.96	0.75	0.250	12	2.63	7.7
	848.9618	2 <sub>1,2</sub> –1 <sub>1,1</sub>	84	$9.27 \times 10^{-4}$	HIFI 3a	25.4	0.96	0.75	0.176	10	3.92	10.3
	893.6387	1 <sub>1,1</sub> –0 <sub>0,0</sub>	43	$8.35 \times 10^{-3}$	HIFI 3b	24.1	0.96	0.74	0.167	63	-2.38 <sup>(4)</sup>	5.9 <sup>(5)</sup>
	919.3109	2 <sub>0,2</sub> –1 <sub>0,1</sub>	66	$1.56 \times 10^{-3}$	HIFI 3b	23.4	0.96	0.74	0.163	20	2.01	6.1
p-H <sub>2</sub> <sup>18</sup> O	203.4075	3 <sub>1,3</sub> –2 <sub>2,0</sub>	204	$4.81 \times 10^{-6}$	IRAM-30m	12.1	0.93	0.62	0.074	121	8.38 <sup>(6)</sup>	5.6 <sup>(6)</sup>
p-H <sub>2</sub> <sup>18</sup> O <sup>(7)</sup>	1101.6983	1 <sub>1,1</sub> –0 <sub>0,0</sub>	53	$1.79 \times 10^{-2}$	HIFI 4b	19.2	0.96	0.74	0.136	110	-1.97 <sup>(8)</sup>	6.4 <sup>(9)</sup>
o-H <sub>2</sub> <sup>18</sup> O <sup>(7)</sup>	547.6764	1 <sub>1,0</sub> –1 <sub>0,1</sub>	60	$3.29 \times 10^{-3}$	HIFI 1a	38.7	0.96	0.75	0.274	12	1.77 <sup>(10)</sup>	7.5 <sup>(11)</sup>

<sup>(1)</sup> The frequencies, upper energy levels ( $E_{up}$ ) and Einstein coefficients ( $A_{ij}$ ) come from the spectroscopic catalog JPL (Pickett et al. 1998).

<sup>(2)</sup> The  $rms$  is calculated at the spectral resolution of the observations, which is indicated in the column  $dv$ .

<sup>(3)</sup> This value corresponds to the ratio between the main beam efficiency  $B_{eff}$  and the forward efficiency  $F_{eff}$ .

<sup>(4)</sup> The integrated flux of the emission component is  $\sim 0.87$  K.km s<sup>-1</sup>, whereas it is  $\sim -3.25$  K.km s<sup>-1</sup> for the absorbing component.

<sup>(5)</sup> The Full Width at Half Maximum ( $FWHM$ ) of the fundamental line at 894 GHz is estimated to be 5.9 km s<sup>-1</sup> for the emission component ( $v_{LSR} = 58.0$  km s<sup>-1</sup>) and 3.9 km s<sup>-1</sup> for the absorption component ( $v_{LSR} = 60.6$  km s<sup>-1</sup>).

<sup>(6)</sup> After subtraction of the CH<sub>3</sub>OCH<sub>3</sub> line contaminating the para-H<sub>2</sub><sup>18</sup>O line profile.

<sup>(7)</sup> Observations from Flagey et al. (2013).

<sup>(8)</sup> The integrated flux of the emission component is  $\sim 1.80$  K km s<sup>-1</sup>, whereas it is  $\sim -0.13$  K km s<sup>-1</sup> for the absorbing component.

<sup>(9)</sup> The Full Width at Half Maximum ( $FWHM$ ) of the fundamental H<sub>2</sub><sup>18</sup>O line at 1101 GHz is estimated to be 6.4 km s<sup>-1</sup> for the emission component ( $v_{LSR} = 57.5$  km s<sup>-1</sup>) and 3.5 km s<sup>-1</sup> for the absorption component ( $v_{LSR} = 61.2$  km s<sup>-1</sup>).

<sup>(10)</sup> The integrated flux of the emission component is  $\sim 1.39$  K km s<sup>-1</sup>, whereas it is  $\sim -3.36$  K km s<sup>-1</sup> for the absorbing component.

<sup>(11)</sup> The Full Width at Half Maximum ( $FWHM$ ) of the fundamental H<sub>2</sub><sup>18</sup>O line at 547 GHz is estimated to be 7.5 km s<sup>-1</sup> for the emission component ( $v_{LSR} = 57.3$  km s<sup>-1</sup>) and 3.3 km s<sup>-1</sup> for the absorption component ( $v_{LSR} = 60.6$  km s<sup>-1</sup>).

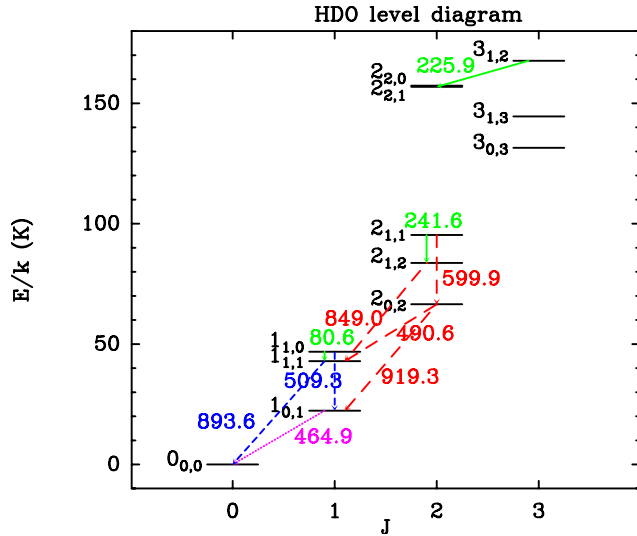


**Figure 1.** Energy level diagram of the HDO lines. Green solid arrows: the IRAM-30m observations; blue short dashed arrows: the PRISMAS/HIFI observations; red long dashed arrows: the Open Time HIFI observations; magenta dotted arrow: the CSO observation. The frequencies are given in GHz. (A color version of this figure is available in the online journal.)

with optimization of the continuum, providing a spectral resolution of 1.1 MHz over an instantaneous bandwidth of  $4 \times 1$  GHz. To disentangle the lines of interest from the lines in the opposite

sideband, possibly contaminating our observations, we observed the same transition with 3 different Local Oscillator (LO) settings. This method is necessary in such chemically rich regions in order to ensure genuine detection of spectral lines. The HDO data were processed using the standard HIFI pipeline up to level 2 with the ESA-supported package HIPE 8.0 (Ott 2010) and were then exported as FITS files into CLASS/GILDAS format<sup>1</sup> for subsequent data reduction. The two linear polarizations were averaged to lower the noise in the final spectrum. The baselines are well-fitted by straight lines over the frequency range of the whole band and were subtracted from all observations. The single sideband continuum temperature (that was obtained by dividing by 2 the DSB continuum derived from the linear fit obtained from line free regions in the spectrum, i.e. assuming a sideband gain ratio of unity) was added to the spectrum of the 1<sub>1,1</sub>–0<sub>0,0</sub> fundamental line. To constrain the HDO/H<sub>2</sub>O ratio, we also used two H<sub>2</sub><sup>18</sup>O transitions observed in the framework of the PRISMAS program and previously published by Flagey et al. (2013). We refer to this paper for the data reduction of these two lines. A list of all the *Herschel*/HIFI observations used in this paper is provided in Table A1.

The ground state 1<sub>0,1</sub>–0<sub>0,0</sub> HDO transition was observed at the Caltech Submillimeter Observatory (CSO) in September 2011 using the Fast Fourier Transform Spectrometer (FFTS) with 500 MHz bandwidth. The data were taken under good weather conditions, with 1.5 mm of precipitable water vapor. The beam switching mode has been used with a chop throw of 240 $''$ . The main beam efficiency

<sup>1</sup> <http://www.iram.fr/IRAMFR/GILDAS>

was determined from total power observations of Mars. The system temperature was about 3500 K during the run. The single sideband continuum temperature ( $\sim 2.2$  K) was added to the final baseline-subtracted spectrum.

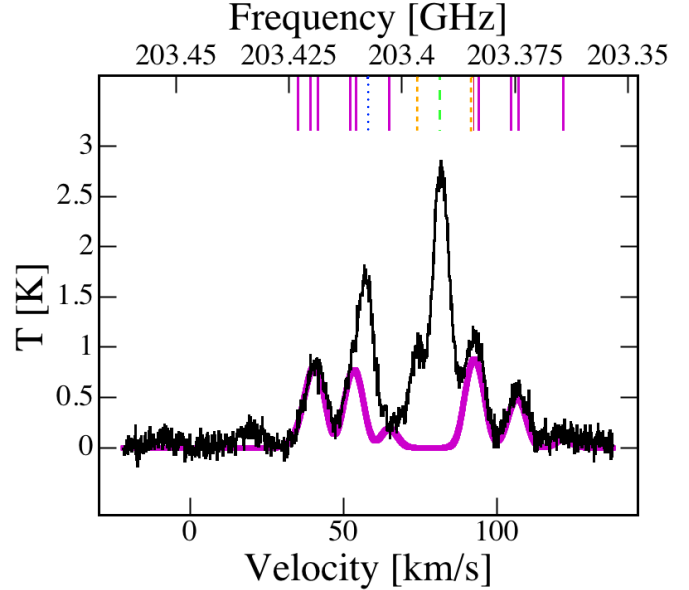
Three additional HDO transitions at 81 ( $1_{1,0}-1_{1,1}$ ), 226 ( $3_{1,2}-2_{2,1}$ ) and 242 GHz ( $2_{1,1}-2_{1,2}$ ) as well as the ortho- $\text{H}_2^{18}\text{O}$  transition at 203 GHz ( $3_{1,3}-2_{2,0}$ ) were observed with the IRAM-30m telescope. The observations were carried out in December 2011 using the Fast Fourier Transform Spectrometer (FTS) at a 50 kHz resolution. The spectral resolution was 0.19, 0.07 and 0.06  $\text{km s}^{-1}$  for the 81, 226 and 242 GHz transitions, respectively. All the observations were performed using the Wobbler Switching mode. The 30m beam sizes at the observing frequencies are given in Table 1. During this run, weather conditions were good for winter, with 2 mm of precipitable water vapor. System temperatures were always less than 200 K.

Figure 1 presents the energy level diagram of the HDO transitions used for the modeling. Table 1 summarizes the observations.

### 3.2 Description of the observations

Most of the observed HDO lines show a Gaussian-like profile (see for example Fig. 4). Only the HDO  $1_{1,1}-0_{0,0}$  fundamental transition observed with *Herschel*/HIFI shows an inverse P-Cygni profile, i.e. a profile showing a red-shifted absorption component and a blue-shifted emission component. A similar profile has already been observed for this transition in low-mass protostars (Coutens et al. 2012, 2013). The Gaussian FWHM (Full Width at Half-Maximum) was derived for each line with the CASSIS<sup>2</sup> software (see Table 1). Using the available spectroscopic databases CDMS (Cologne Database Molecular Spectroscopy; Müller et al. 2011, 2005) and JPL (Jet Propulsion Laboratory; Pickett et al. 1998), we also checked that the different lines are not contaminated by other species. The HDO  $2_{1,1}-2_{1,2}$  transition at 242 GHz could be slightly blended with the  $\text{CH}_3\text{COCH}_3$   $13_{10,4}-12_{9,3}$  line. However a simple LTE (Local Thermal Equilibrium) modeling of  $\text{CH}_3\text{COCH}_3$  lines observed in the spectra, shows that the contribution of  $\text{CH}_3\text{COCH}_3$  is negligible. With a column density of  $4 \times 10^{16} \text{ cm}^{-2}$ , an excitation temperature of 100 K, a FWHM of 6  $\text{km s}^{-1}$  and a source size of 1.7'', the predicted intensity of the  $\text{CH}_3\text{COCH}_3$  line at 241.6 GHz is 0.06 K, to be compared with the observed line intensity 1.75 K. The HDO  $2_{1,2}-1_{1,1}$  line at 849 GHz is very probably blended with three  $^{13}\text{CH}_3\text{OH}$  lines ( $18_{3,15}-17_{3,14}$  A-,  $18_{4,14}-17_{4,13}$  A+, and  $18_{4,15}-17_{4,14}$  A-) lying in the red-shifted portion of the line profile. This could explain why this line is broader than the others (see Table 1). As the  $^{13}\text{CH}_3\text{OH}$  contribution could be non-negligible, we do not use this HDO line to constrain the abundances. We present however the modeling of this line for completeness. The other HDO lines do not show any potential blending. The portion of the 600 GHz line observed at  $v > 72 \text{ km s}^{-1}$  is produced by the  $\text{CH}_3\text{OH}$   $7_{3,5}-6_{2,4}$   $v=0$  A+ line from the image band ( $v = 590.3 \text{ GHz}$ ).

The para- $\text{H}_2^{18}\text{O}$   $3_{1,3}-2_{2,0}$  line is blended with the  $\text{CH}_3\text{OCH}_3$   $3_{3,1,1}-2_{2,1,1}$  and  $3_{3,0,3}-2_{2,1,3}$  transitions at 203.4101 and 203.4114 GHz ( $E_{\text{up}} = 18 \text{ K}$ ). We can reproduce, with a LTE modeling approach, the  $\text{CH}_3\text{OCH}_3$  lines observed nearby in the spectra (see Figure 2) as well as in the other bands. The  $\text{CH}_3\text{OCH}_3$  lines are well-fitted with a column density of  $7 \times 10^{17} \text{ cm}^{-2}$ , an excitation temperature of 100 K, a FWHM of 6  $\text{km s}^{-1}$  and a source size of 1.7''. The predicted line profiles of the  $\text{CH}_3\text{OCH}_3$  transitions blended with  $\text{H}_2^{18}\text{O}$  are then subtracted from the



**Figure 2.** IRAM-30m observations (in black) of the para- $\text{H}_2^{18}\text{O}$   $3_{1,3}-2_{2,0}$  transition at 203.4 GHz. The frequency of the  $\text{H}_2^{18}\text{O}$  line is indicated by a blue dotted line ( $v = 58 \text{ km s}^{-1}$ ). The other lines observed in this spectra are the  $\text{SO}_2$   $v=0$   $12_{0,12}-11_{1,11}$  line at 81.5  $\text{km s}^{-1}$  (green long dashed line), the  $\text{C}_2\text{H}_5\text{CN}$   $v=0$   $23_{2,22}-22_{2,21}$  line at 74.1  $\text{km s}^{-1}$  (yellow short dashed line) and several  $\text{CH}_3\text{OCH}_3$  lines (magenta solid lines). A LTE modeling of the  $\text{CH}_3\text{OCH}_3$  lines (in magenta) was carried out to estimate the contamination of the para- $\text{H}_2^{18}\text{O}$  line by the  $\text{CH}_3\text{OCH}_3$   $3_{3,1,1}-2_{2,1,1}$  transition. (A color version of this figure is available in the online journal.)

observed line profile to extract the proper  $\text{H}_2^{18}\text{O}$  spectrum. Due to the high number of  $\text{CH}_3\text{OCH}_3$  lines considered in the analysis and the presence of  $\text{CH}_3\text{OCH}_3$  lines with similar upper energy levels (18 K) around the  $\text{H}_2^{18}\text{O}$  feature (see Figure 2), the uncertainty produced by this subtraction is negligible with respect to the calibration uncertainty ( $\leq 20\%$ ).

## 4 RADIATIVE TRANSFER MODELING

### 4.1 Rotational diagram analysis

A simple LTE modeling was first employed to estimate the HDO/ $\text{H}_2\text{O}$  ratio in the hot core. We plot in Figure 3 the rotation diagram (Goldsmith & Langer 1999) of the HDO lines shown in Table 1. We exclude the fundamental transition at 894 GHz, which shows absorption and probably probes colder regions outside of the hot core. We take into account beam dilution and consider different source sizes between 1'' and 5'', as the exact size of the hot core is unknown. Indeed, the structure determined by van der Tak et al. (2013) predicts a size of 4.5'' for  $T > 100 \text{ K}$ , whereas the interferometric observations of two HDO lines by Liu et al. (2013) favor a smaller source size which, however, is not well constrained. No linear curve is in reasonable agreement with the complete dataset. Plausible explanations are that the lines are optically thick or that they do not all have the same excitation temperature. We estimate the critical densities of these species using the HDO collisional coefficients with ortho- and para- $\text{H}_2$  of Faure et al. (2011). At  $\sim 100 \text{ K}$ , the critical densities are about  $5 \times 10^6 - 5 \times 10^7 \text{ cm}^{-3}$  for all lines, except for the lines at 80, 226, and 242 GHz that have critical densities between  $3 \times 10^4$  and  $3 \times 10^5 \text{ cm}^{-3}$ . These latter lines

<sup>2</sup> <http://cassis.irap.omp.eu>

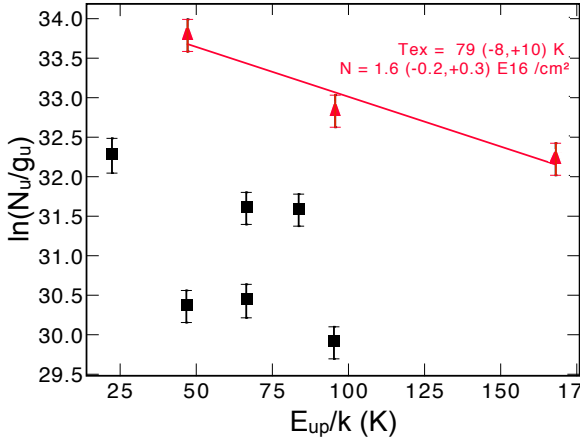


**Figure 3.** Rotational diagram of the HDO lines. The fundamental line at 894 GHz is excluded from the figure. A source size of  $4''$  is assumed. The error bars correspond to uncertainties of 20%. A linear fit was made using only the lines with low critical densities (81, 226, and 242 GHz, indicated by red triangles) to estimate the HDO column density ( $\sim 1.6 \times 10^{16} \text{ cm}^{-2}$ ) and the excitation temperature ( $\sim 79 \text{ K}$ ) in the hot core (see text). (A color version of this figure is available in the online journal.)

are at low frequencies, so that their radiative decay is slower. They are consequently probably in LTE, as the density in the hot core is expected to be  $\geq 10^6 \text{ cm}^{-3}$  (van der Tak et al. 2013). In addition, these three lines are also those with the expected lowest opacities. We consequently fit a straight line to these three points only. The column density and the excitation temperature of HDO were then estimated for different values of the source size ( $1''$ – $5''$ ). To derive the HDO/H<sub>2</sub>O ratio, we used the H<sub>2</sub><sup>18</sup>O  $3_{1,3}$ – $2_{2,0}$  line observed at 203 GHz with IRAM. Indeed this line is quite excited and its critical density is relatively low, about  $10^5 \text{ cm}^{-3}$ . Using the same excitation temperature as HDO, we calculated the column density of H<sub>2</sub><sup>18</sup>O in the hot core and derived an estimate of the HDO/H<sub>2</sub>O ratio between  $5.2 \times 10^{-4}$  and  $5.7 \times 10^{-4}$ . The H<sub>2</sub><sup>16</sup>O/H<sub>2</sub><sup>18</sup>O ratio is assumed to be 400 following the relation determined by Wilson (1999) between the <sup>16</sup>O/<sup>18</sup>O isotopic ratio and the distance of the source from the galactic center. The derived HDO/H<sub>2</sub>O ratio is consistent with the previous estimates by Jacq et al. (1990,  $4 \times 10^{-4}$ ) and Liu et al. (2013,  $3.0 \times 10^{-4}$ ), who assumed an H<sub>2</sub><sup>16</sup>O/H<sub>2</sub><sup>18</sup>O ratio equal to 500. It is also slightly greater than the estimate by Gensheimer et al. (1996,  $1.1 \times 10^{-4}$ ).

## 4.2 Non-LTE spherical modeling

### 4.2.1 Model description

Only three HDO lines (among 10) were used to estimate the HDO/H<sub>2</sub>O ratio in the hot core with the rotational diagram analysis. We consequently decided to employ non-LTE spherical modeling (that also considers the line opacities) to include the information provided by all the HDO lines (except the 848 GHz line that is probably blended with <sup>13</sup>CH<sub>3</sub>OH) and to determine the water deuterium fractionation in both the hot core and the colder part of the envelope. We used the RATRAN code (Hogerheijde & van der Tak 2000) that assumes spherical symmetry and takes into account continuum emission and absorption by dust. To derive the HDO and H<sub>2</sub><sup>18</sup>O abundances, we used the temperature and H<sub>2</sub> density profiles derived by van der Tak et al. (2013, Section 4.1). This structure

was determined taking into account JCMT/SCUBA and PACS data. The radial velocity profile ( $v_r$ ) and the turbulence width (Doppler b-parameter,  $db$ ) have also to be provided in RATRAN. We describe in Appendix B2 the method employed to constrain them and show the final  $v_r$  and  $db$  profiles used in the analysis. We find that inward motions ( $v_r \sim -3 \text{ km s}^{-1}$ ) are present in the cold envelope, while outward motions ( $v_r \sim 4 \text{ km s}^{-1}$ ) take place in the inner regions. The same type of velocity profile was found in SgrB2(M) by Rolfs et al. (2010). The Doppler b-parameter appears lower in the inner regions ( $db \sim 2.0 \text{ km s}^{-1}$ ) than in the outer regions ( $db \sim 2.5 \text{ km s}^{-1}$ ), similarly to what was found by Caselli & Myers (1995) and Herpin et al. (2012) in other high mass sources. To reproduce the continuum levels seen in the observations as best as possible, we used the dust opacities from Ossenkopf & Henning (1994), with thick ice mantles and a gas density of  $10^6 \text{ cm}^{-3}$ . The dust opacities used by van der Tak et al. (2013, thin ices mantles with gas density of  $10^6 \text{ cm}^{-3}$ ) to derive the structure would not however differ too much, as the predicted continuum is consistent with the observations to within 10–20% uncertainties. The most recent HDO and H<sub>2</sub><sup>18</sup>O collisional coefficients calculated with ortho- and para-H<sub>2</sub> by Faure et al. (2011) and Daniel et al. (2011), respectively, were used. The ortho/para ratio of H<sub>2</sub> is assumed to be at LTE in each cell of the envelope. It consequently varies from  $\sim 10^{-2}$  in the coldest regions up to the equilibrium value of 3 in the warm regions.

### 4.2.2 Modeling of the HDO lines with an abundance jump

Most of the studies of water and deuterated water in star-forming regions (e.g., Ceccarelli et al. 2000; Parise et al. 2005; van der Tak et al. 2006; Coutens et al. 2012; Herpin et al. 2012) assume an abundance jump at  $T_j = 100 \text{ K}$ , corresponding to the temperature at which the water molecules are supposed to be released in the gas phase by thermal desorption. In a first step, we consequently assumed such an abundance jump for the modeling of the HDO lines. According to the physical structure used here (van der Tak et al. 2013), the source size corresponding to  $T > 100 \text{ K}$  is  $\sim 4.5''$  (diameter). We ran a grid of models with various inner ( $T > 100 \text{ K}$ ) and outer ( $T < 100 \text{ K}$ ) abundances and realized that, regardless of the velocity profiles, the intensities of the different lines cannot be reproduced simultaneously (see Figure 4). Indeed, when the excited transitions observed at 225 and 241 GHz with IRAM are reproduced, the fluxes of the CSO and HIFI lines are overproduced, in particular at 491, 600, 849, and 919 GHz (red dashed model in Figure 4). On the contrary, if these latter lines are reproduced, the flux is underpredicted for the IRAM lines (green dotted model in Figure 4). Although the choice of the velocity profiles can affect the line profiles, it is not possible to appreciably modify the intensities and decrease this disagreement.

To obtain an agreement for all the transitions, an increase of the jump temperature is necessary. Indeed, Figure B4 shows that, with a jump temperature of 120 K, the model that reproduces the fluxes of the most excited HDO lines (226 and 242 GHz) is in better agreement with the fluxes of the lines at 491, 600, 849, and 919 GHz than the model with a jump at  $T_j = 100 \text{ K}$ . The fluxes of these four lines are, however, still overproduced. Consequently, we ran grid of models for higher jump temperatures (150, 180, 200, and 220 K) and compared the influence of the jump temperature on the line intensities. The best-fit predictions obtained for  $T_j = 150 \text{ K}$ , 180 K, 200 K, and 220 K are shown in Figures B5, B6, 5, and B7, respectively. These four models reproduce relatively well the observations. The 491, 600, 849, and 919 GHz lines are quite sensitive to the jump temperature. Their intensities decrease with the



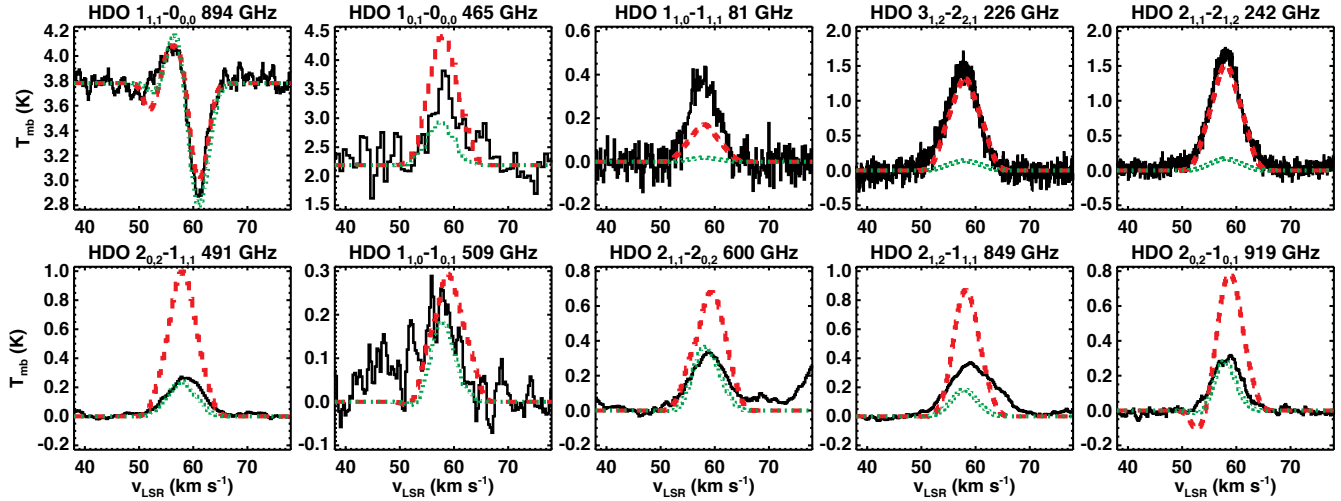


**Figure 4.** Black solid line: HDO lines observed with HIFI, IRAM, and CSO. Red dashed line: Modeling for a jump temperature  $T_j = 100$  K, an inner abundance  $X_{in} = 3 \times 10^{-8}$  and an outer abundance  $X_{out} = 8 \times 10^{-11}$ . Green dotted line: Modeling for a jump temperature  $T_j = 100$  K, an inner abundance  $X_{in} = 3 \times 10^{-9}$  and an outer abundance  $X_{out} = 8 \times 10^{-11}$ . (A color version of this figure is available in the online journal.)

increase of  $T_j$ . In particular, for  $T_j = 150$  K and  $180$  K, their intensities are slightly overpredicted, while, for  $T_j \geq 220$  K, they start to be under-predicted. In view of these results, the best-fit model is obtained for  $T_j \sim 200$  K. Table 2 summarizes the HDO best-fit abundances found for each jump temperature and the corresponding size of the jump abundance. The best-fit was determined with a  $\chi^2$  minimization of the line profiles similar to what was done in Coutens et al. (2012), assuming a calibration uncertainty of 20% for each line. As the HDO line at  $849$  GHz is probably blended with  $^{13}\text{CH}_3\text{OH}$ , we did not include it in the calculation. The reduced  $\chi^2$  obtained for the model with an abundance jump at  $200$  K is  $1.3$ . The HDO inner abundance is strongly constrained by the high number of emission lines used in the analysis. If we just consider the grid with  $T_j = 200$  K, its value is between  $1.7 \times 10^{-7}$  and  $2.1 \times 10^{-7}$ . Consequently, the main uncertainty on the HDO inner abundance comes from the value assumed for the jump temperature ( $\sim 1 \times 10^{-7} - 3 \times 10^{-7}$  for  $T_j \sim 150 - 220$  K). The outer abundance is mainly constrained by the absorbing component at  $894$  GHz and its uncertainty is found to be between  $6 \times 10^{-11}$  and  $9 \times 10^{-11}$ . The HDO  $1_{1,0} - 1_{1,1}$  line at  $81$  GHz is not reproduced by any of the models within the 20% calibration uncertainty and could maybe suffer of calibration problems at this low frequency with the IRAM-30m telescope. Models with a two-jump abundance profile such as in Comito et al. (2010) were also attempted but do not improve the fit (see Appendix B3).

It clearly appears that, to reproduce the HDO line profiles, an increase of the jump temperature in the model is necessary. We cannot conclude, however, that the sublimation temperature for water ice is significantly higher than  $100$  K. Although some experiments actually favor an evaporation temperature of  $110 - 120$  K (Fraser et al. 2001), it is not sufficient to perfectly reproduce all the HDO transitions. The main reason for the modification of the jump temperature would be related to the size of the hot core, rather than to the water sublimation temperature itself. In this case, the size of the hot core in which the abundance of water increases after the evaporation of the icy mantles should be smaller ( $\sim 2''$  instead of  $4.5''$ ), in order to lead to a better agreement between the model and the observations. This is also in agreement with the interferometric ob-

servations of the HDO lines at  $225$  and  $241$  GHz by Liu et al. (2013) that are not spatially resolved with a beam size of  $3.7'' \times 2.5''$ . Two explanations can be provided to explain the smaller size of the hot core. One would be that the physical structure derived by van der Tak et al. (2013) is unreliable at small scales. Indeed the structure determined here is only based on large-scale maps and the density profile is assumed to follow a power-law. The density and temperature profiles could therefore be uncertain at small scales ( $\theta \lesssim 5''$ ). In this case, the temperature actually would reach  $100$  K at a radius which is smaller than what the physical structure predicts (van der Tak et al. 2013). The second possible explanation is provided by the chemical models coupled with a dynamical approach, where the dynamical timescales can be in competition with the chemical and adsorption/desorption timescales. Indeed, as it can be seen for example in Aikawa et al. (2012) and Wakelam et al. (submitted), the abundance increases gradually for a certain temperature range before a constant inner abundance is reached. The temperature where the inner abundance is constant is higher than  $100$  K but its exact value is dependent on the model parameters. It seems therefore possible that the constant inner abundance can be reached only at  $\sim 200$  K. Some tests assuming a gradual abundance increase were attempted in Section 4.2.5 and this explanation seems to hold here.

#### 4.2.3 Modeling of the $\text{H}_2^{18}\text{O}$ lines with an abundance jump and estimate of the HDO/ $\text{H}_2\text{O}$ ratios

A similar model with an abundance jump was carried out with the  $\text{H}_2^{18}\text{O}$  lines detected in this source to determine the HDO/ $\text{H}_2\text{O}$  ratio throughout the envelope. The  $\text{H}_2^{16}\text{O}$  transitions detected with the HIFI instrument by Flagey et al. (2013) are not well suited to measure abundances, because of their large opacities. With its excitation level, the para- $\text{H}_2^{18}\text{O}$   $3_{1,3} - 2_{2,0}$  transition observed at  $203$  GHz with the IRAM-30m telescope is suitable to probe the hot core and derive the HDO/ $\text{H}_2\text{O}$  ratio in the warm inner region. The  $\text{H}_2^{18}\text{O}$  fundamental lines previously detected with *Herschel*/HIFI by Flagey et al. (2013) are also used to constrain the HDO/ $\text{H}_2\text{O}$  ratio in the envelope, as these lines combine both emission and absorption. Note

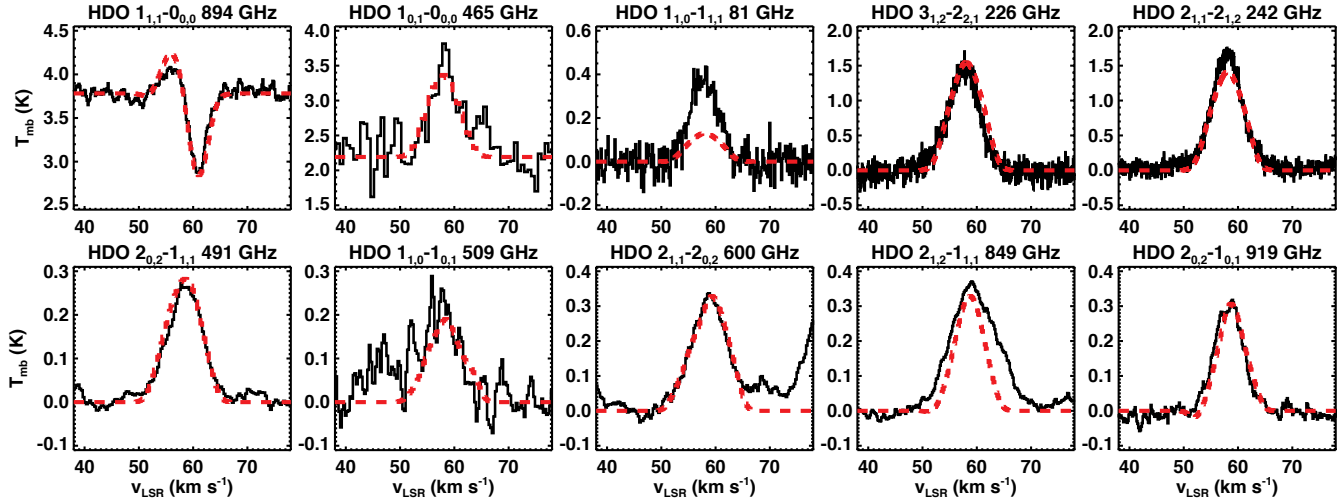


**Figure 5.** Black solid line: HDO lines observed with HIFI, IRAM, and CSO. Red dashed line: Modeling for a jump temperature  $T_j = 200$  K, an inner abundance  $X_{in} = 2 \times 10^{-7}$  and an outer abundance  $X_{out} = 8 \times 10^{-11}$ . (A color version of this figure is available in the online journal.)

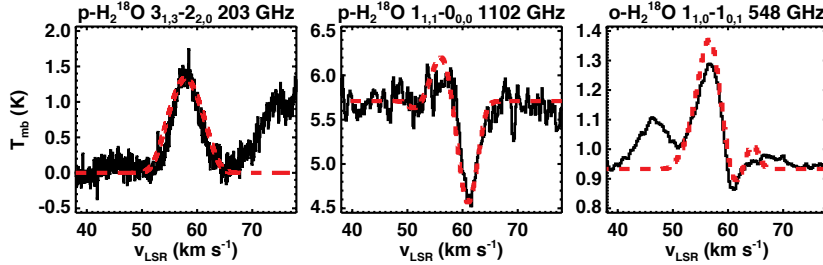


**Figure 6.** Black solid line:  $\text{H}_2^{18}\text{O}$  lines observed with HIFI and IRAM. Red dashed line: Modeling for a jump temperature  $T_j = 200$  K, an inner abundance  $X_{in} = 9 \times 10^{-7}$  and an outer abundance  $X_{out} = 1.3 \times 10^{-10}$ . (A color version of this figure is available in the online journal.)

that we only use here the ortho  $1_{1,0}-1_{0,1}$  transition at 548 GHz and the para  $1_{1,1}-0_{0,0}$  transition at 1102 GHz. The fundamental ortho  $2_{1,2}-1_{0,1}$  transition, which is observed at 1656 GHz in absorption, was not taken into account because of pointing problems affecting the observations. The source being fairly peaked on the continuum, an offset could lead to a significant loss of flux.

All the physical parameters are kept similar to those of the study of HDO. Figures B8, B9, 6, and B10 show the best-fit models obtained for these three lines for the jump temperatures previously assumed for deuterated water,  $T_j = 150, 180, 200$ , and  $220$  K respectively. We assumed an ortho-to-para ratio of water equal to 3, corresponding to the thermal equilibrium value at high-temperature ( $> 50$  K). This value is also consistent with the ratio determined in most of the foreground clouds on the line of sight towards bright continuum sources (Lis et al. 2010; Flagey et al. 2013). The best-fit inner and outer  $\text{H}_2^{18}\text{O}$  abundances are summarized in Table 2. The reduced  $\chi^2$  is about 1.5 for the case  $T_j = 200$  K. Assuming an observational uncertainty of 20% for the excited para- $\text{H}_2^{18}\text{O}$  line at 203 GHz, the inner abundance cannot be higher than  $1.2 \times 10^{-6}$  or lower than  $7 \times 10^{-7}$  for the model with  $T_j = 200$  K. The outer abundance is estimated to be between  $1.0 \times 10^{-10}$  and  $1.5 \times 10^{-10}$ , based on an observational uncertainty of 20% for the absorbing component of the para- $\text{H}_2^{18}\text{O}$  transition at 1102 GHz. The  $\text{H}_2^{16}\text{O}$  abundances in Table 2 are estimated using an  $\text{H}_2^{16}\text{O}/\text{H}_2^{18}\text{O}$  ratio of 400 (Wilson 1999).

The best-fit HDO/ $\text{H}_2\text{O}$  ratios are then equal to  $\sim (5-6) \times 10^{-4}$  in the hot core and  $\sim 1.5 \times 10^{-3}$  in the outer envelope. Even when considering the HDO and  $\text{H}_2^{18}\text{O}$  results with a 20% calibration uncertainty, the outer HDO/ $\text{H}_2\text{O}$  ratio ( $1.0 \times 10^{-3} - 2.2 \times 10^{-3}$ ) is still higher than the inner HDO/ $\text{H}_2\text{O}$  ratio ( $3.5 \times 10^{-4} - 7.5 \times 10^{-4}$  for  $T_j = 200$  K). We ran models with a constant ortho/para  $\text{H}_2$  ratio equal to 3 to check that the ortho/para  $\text{H}_2$  ratio assumed in the model does not affect the results. The HDO and  $\text{H}_2^{18}\text{O}$  line profiles are exactly the same as with an LTE ortho/para ratio, confirming the variation of the HDO/ $\text{H}_2\text{O}$  ratio from the cold to the warm regions.

#### 4.2.4 Gradual decrease of the outer abundance from the cold to the warm regions

Although we used a constant abundance of HDO and  $\text{H}_2^{18}\text{O}$  in the cold envelope of G34, it is very probable that the water abundance shows variations in this region due to non-thermal desorption mechanisms. In particular, Mottram et al. (2013) showed that the desorption by the cosmic ray-induced UV field leads to an outer abundance of water decreasing gradually from the cold to the warm regions of low-mass protostars. To confirm that the presence of a gradual abundance decrease in the cold envelope does not affect the derived value of the HDO/ $\text{H}_2\text{O}$  ratio in this region, we ran a modeling considering an equilibrium state between the desorption by the cosmic ray-induced UV field and the re-depletion on the grains.

**Table 2.** HDO and H<sub>2</sub>O abundances obtained for different jump temperatures  $T_j$ 

$T_j$ (K) <sup>(a)</sup>	$\theta$ (") <sup>(a)</sup>	$X_{\text{in}}(\text{HDO})$	$X_{\text{out}}(\text{HDO})$	$X_{\text{in}}(\text{H}_2^{18}\text{O})$	$X_{\text{out}}(\text{H}_2^{18}\text{O})$	$X_{\text{in}}(\text{H}_2\text{O})^{(b)}$	$X_{\text{out}}(\text{H}_2\text{O})^{(b)}$	$(\text{HDO}/\text{H}_2\text{O})_{\text{in}}^{(b)}$	$(\text{HDO}/\text{H}_2\text{O})_{\text{out}}^{(b)}$
100 <sup>(c)</sup>	4.5	–	–	–	–	–	–	–	–
120 <sup>(c)</sup>	3.5	–	–	–	–	–	–	–	–
150	2.5	$1 \times 10^{-7}$	$8 \times 10^{-11}$	$4 \times 10^{-7}$	$1.3 \times 10^{-10}$	$1.6 \times 10^{-4}$	$5.2 \times 10^{-8}$	$6 \times 10^{-4}$	$1.5 \times 10^{-3}$
180	1.9	$1.5 \times 10^{-7}$	$8 \times 10^{-11}$	$7 \times 10^{-7}$	$1.3 \times 10^{-10}$	$2.8 \times 10^{-4}$	$5.2 \times 10^{-8}$	$5 \times 10^{-4}$	$1.5 \times 10^{-3}$
<b>200<sup>(d)</sup></b>	<b>1.7</b>	<b><math>2 \times 10^{-7}</math></b>	<b><math>8 \times 10^{-11}</math></b>	<b><math>9 \times 10^{-7}</math></b>	<b><math>1.3 \times 10^{-10}</math></b>	<b><math>3.6 \times 10^{-4}</math></b>	<b><math>5.2 \times 10^{-8}</math></b>	<b><math>6 \times 10^{-4}</math></b>	<b><math>1.5 \times 10^{-3}</math></b>
220	1.5	$3 \times 10^{-7}$	$8 \times 10^{-11}$	$1.2 \times 10^{-6}$	$1.3 \times 10^{-10}$	$4.8 \times 10^{-4}$	$5.2 \times 10^{-8}$	$6 \times 10^{-4}$	$1.5 \times 10^{-3}$

Notes: <sup>(a)</sup> Size of the region where the temperature is higher than  $T_j$  (diameter). It is derived from the structure determined by van der Tak et al. (2013). <sup>(b)</sup> Assuming  $\text{H}_2^{16}\text{O}/\text{H}_2^{18}\text{O} = 400$ . <sup>(c)</sup> Fit is not good enough to determine the HDO abundances. <sup>(d)</sup> Best-fit.

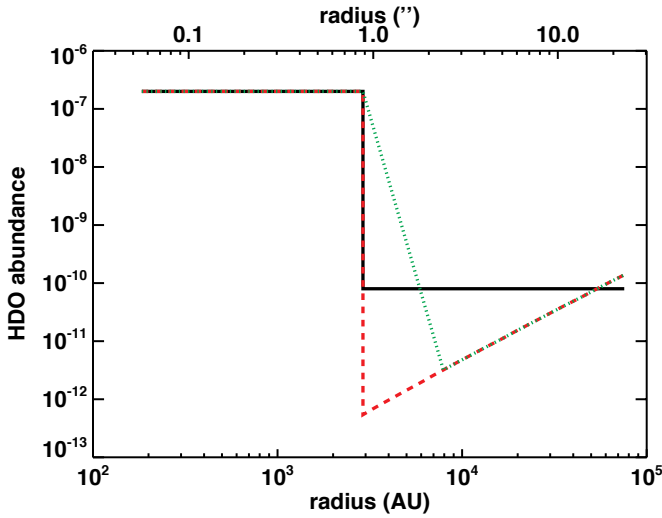


**Figure 7.** Best-fit abundance profiles obtained for HDO when the outer abundance (region at  $T < 200$  K) is constant (black solid line, Section 4.2.2), when it decreases from the cold regions to the region at  $T = 200$  K (red dashed line, Section 4.2.4), and when it decreases from the cold regions to the region at  $T = 100$  K and increases from  $T = 100$  K to  $T = 200$  K (green dotted line, see Section 4.2.5). The temperature reaches 200 K at a radius of 2700 AU ( $\sim 0.9''$ , see Figure B1). (A color version of this figure is available in the online journal.)

Using similar equations to those in Hollenbach et al. (2009) and Mottram et al. (2013), we get by equating desorption to depletion:

$$G_{\text{cr}} F_0 Y_x f_{s,x} n_{\text{gr}} \sigma_{\text{gr}} = n(x) n_{\text{gr}} \sigma_{\text{gr}} v_{\text{th},x} \quad (4)$$

with  $F_0$  the local interstellar flux of 6–13.6 eV photons assumed to be equal to  $10^8$  photons  $\text{cm}^{-2} \text{s}^{-1}$ ,  $G_{\text{cr}}$  the scaling factor of the UV flux,  $Y_x$  the photodesorption yield for the molecule  $x$  ( $\sim 10^{-3}$  for H<sub>2</sub>O, Öberg et al. 2009),  $f_{s,x}$  the fraction of the molecule  $x$  on grains,  $n_{\text{gr}}$  the grain density,  $\sigma_{\text{gr}}$  the cross sectional area of the grain and  $v_{\text{th},x}$  the thermal velocity. The thermal velocity is calculated according to the following formalism:

$$v_{\text{th},x} = \sqrt{\frac{8k_b T_k}{\pi m_x}}, \quad (5)$$

where  $k_b$  is the Boltzmann constant,  $T_k$  the gas temperature and  $m_x$  the mass of the molecule  $x$ . The outer abundance of H<sub>2</sub>O with respect to H<sub>2</sub> is then equal to:

$$X_{\text{out}}(\text{H}_2\text{O}) = \frac{G_{\text{cr}} F_0 Y_{\text{H}_2\text{O}} f_{s,\text{H}_2\text{O}}}{v_{\text{th},\text{H}_2\text{O}} n_{\text{H}_2}}, \quad (6)$$

with  $n_{\text{H}_2}$  the H<sub>2</sub> density. Similarly we obtain for HDO:

$$X_{\text{out}}(\text{HDO}) = \frac{G_{\text{cr}} F_0 Y_{\text{HDO}} f_{s,\text{H}_2\text{O}}}{v_{\text{th},\text{HDO}} n_{\text{H}_2}} \left( \frac{\text{HDO}}{\text{H}_2\text{O}} \right), \quad (7)$$

and for H<sub>2</sub><sup>18</sup>O:

$$X_{\text{out}}(\text{H}_2^{18}\text{O}) = \frac{G_{\text{cr}} F_0 Y_{\text{H}_2^{18}\text{O}} f_{s,\text{H}_2\text{O}}}{v_{\text{th},\text{H}_2^{18}\text{O}} n_{\text{H}_2}} \left( \frac{\text{H}_2^{18}\text{O}}{\text{H}_2\text{O}} \right). \quad (8)$$

The photodesorption yields for HDO and H<sub>2</sub><sup>18</sup>O are assumed similar to those for H<sub>2</sub>O (Öberg et al. 2009). The thermal velocity is approximatively the same due to their relatively similar masses. All the other parameters are independent of the molecules except the fraction  $f_{s,x}$  of these molecules contained in the grain mantles which reflects the isotopic ratios, HDO/H<sub>2</sub>O and H<sub>2</sub><sup>18</sup>O/H<sub>2</sub><sup>16</sup>O, on the grains. The external UV field should also affect the external part of the outer envelope. But, due to the very small constraints on these different mechanisms, we only considered the desorption by the cosmic ray-induced UV field.

We ran a grid of models for the case  $T_j = 200$  K, keeping the inner abundances determined previously ( $X_{\text{in}}(\text{HDO}) = 2 \times 10^{-7}$  and  $X_{\text{in}}(\text{H}_2^{18}\text{O}) = 9 \times 10^{-7}$ ). Different values were then assumed for the factors  $W_{\text{HDO}} = G_{\text{cr}} f_{s,\text{H}_2\text{O}} \text{HDO}/\text{H}_2\text{O}$  and  $W_{\text{H}_2^{18}\text{O}} = G_{\text{cr}} f_{s,\text{H}_2\text{O}} \text{H}_2^{18}\text{O}/\text{H}_2^{16}\text{O}$ . Assuming  $\text{H}_2^{18}\text{O}/\text{H}_2^{16}\text{O} = 400$  (Wilson 1999) and  $f_{s,\text{H}_2\text{O}} = 1$  (the icy grain mantles are constituted entirely of H<sub>2</sub>O), the best-fit model of the H<sub>2</sub><sup>18</sup>O lines gives a scaling factor  $G_{\text{cr}}$  of about  $1.6 \times 10^{-3}$ . If water represents only 50% of the grain mantles,  $G_{\text{cr}}$  is then equal to  $3.2 \times 10^{-3}$  leading to a cosmic ray-induced UV field of  $\sim 3 \times 10^5$  photons  $\text{cm}^{-2} \text{s}^{-1}$ . These values represent, however, only upper limits, since the desorption by the external UV field is not taken into account in the analysis. The typical value of the cosmic-ray induced UV flux ( $G_{\text{cr}} \sim 10^{-4}$ ; e.g., Prasad & Tarafdar 1983; Shen et al. 2004) is then consistent with the upper limit derived here ( $G_{\text{cr}} \lesssim 3 \times 10^{-3}$ ).

The best-fit abundance profile determined for HDO when the outer abundance decreases from the cold to the warm regions is presented in Figure 7 (red dashed line). The HDO/H<sub>2</sub>O ratio in the outer envelope is equal to  $1.3 \times 10^{-3}$ . It is then, once again, higher than in the hot core ( $\sim (5-6) \times 10^{-4}$ ). The HDO and H<sub>2</sub><sup>18</sup>O line profiles predicted with the RATRAN code (see red dashed lines in Figures 8 and 9) are relatively similar to those in Figures 5 and 6 that assume a two-step abundance profile with a jump at 200 K. The fit is even better for the H<sub>2</sub><sup>18</sup>O and HDO fundamental transitions (HDO: 894 GHz; H<sub>2</sub><sup>18</sup>O: 548 and 1102 GHz), as the predicted intensity of their emission is now in agreement with the observations. Some of the HDO lines (509, 600, and 919 GHz) show small self-absorptions on their blue-shifted side. However, these defects could probably disappear with slightly different velocity profiles. Indeed,



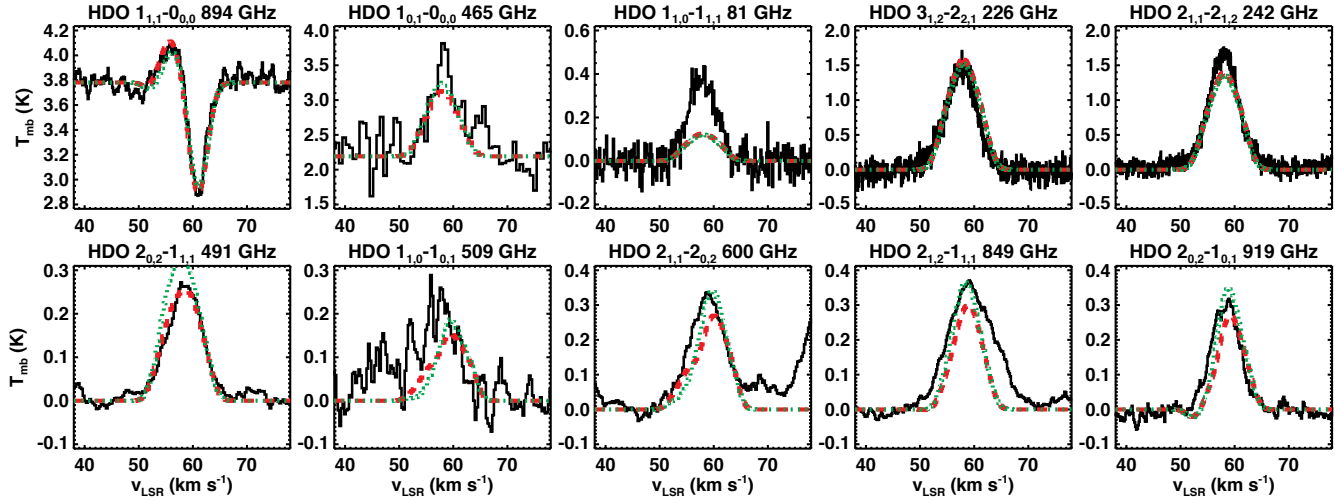


**Figure 8.** Black solid line: HDO lines observed with HIFI, IRAM, and CSO. Red dashed line: Modeling for a constant inner abundance  $X_{\text{in}} = 2 \times 10^{-7}$  ( $T \geq 200$  K) and an outer abundance ( $T < 200$  K) decreasing from the cold to the warm regions (see Section 4.2.4). Green dotted line: Modeling for a constant inner abundance  $X_{\text{in}} = 2 \times 10^{-7}$  ( $T \geq 200$  K), an abundance gradually increasing from 100 to 200 K, and an outer abundance ( $T < 100$  K) decreasing from the cold to the warm regions (see Section 4.2.5). (A color version of this figure is available in the online journal.)

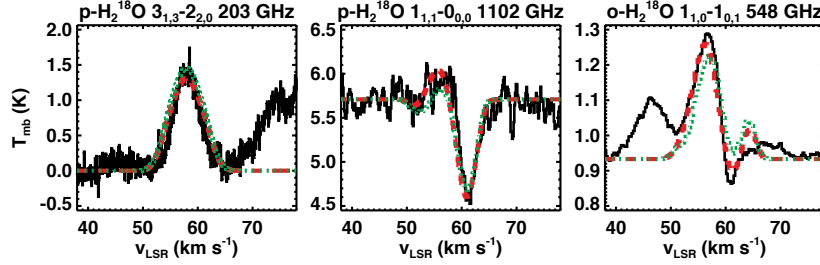


**Figure 9.** Black solid line:  $\text{H}_2^{18}\text{O}$  lines observed with HIFI and IRAM. Red dashed line: Modeling for a constant inner abundance  $X_{\text{in}} = 9 \times 10^{-7}$  ( $T \geq 200$  K) and an outer abundance ( $T < 200$  K) decreasing from the cold to the warm regions (see Section 4.2.4). Green dotted line: Modeling for a constant inner abundance  $X_{\text{in}} = 9 \times 10^{-7}$  ( $T \geq 200$  K), an abundance gradually increasing from 100 to 200 K, and an outer abundance ( $T < 100$  K) decreasing from the cold to the warm regions (see Section 4.2.5). (A color version of this figure is available in the online journal.)

the velocity profiles used here were only adapted for the models with the abundance jumps (see Appendix B2).

#### 4.2.5 Gradual increase of the water abundance profile at the cold envelope/hot core transition

In Section 4.2.2, we mentioned that a model with a gradual increase of the HDO abundance at the cold envelope/hot core transition could potentially explain why we need a higher jump temperature than 100 K to reproduce the HDO line profiles. Here we show the results obtained with both a decrease of the outer abundance from the outermost regions to the regions at 100 K and a gradual increase from 100 to 200 K. This type of profile is then relatively similar to the predictions of chemical models coupled with a dynamical approach (Aikawa et al. 2012, Wakelam et al. submitted). The HDO inner abundance is equal to  $2 \times 10^{-7}$  and the outer abundance follows the trend described in Section 4.2.4. The abundance profile used and the result of the model for HDO are shown in Figures 7 and 8 (green dotted line), respectively. This model also appears very similar to the model with an abundance jump at 200 K (see Figure 5). A model with both an abundance decrease (with temperature) in the colder envelope and an increase of

the abundance towards the hot core is probably more realistic than the jump abundance assumption and could explain why the hot core is smaller than expected. It is, however, important to note that the temperature range of the gradual abundance increase is not known. We assume here the range 100–200 K but it could be slightly different and a specific range is probably dependent on the dynamics. The result of this modeling should thus be considered only qualitatively. We can however conclude that this type of abundance profile allows to reproduce the HDO line profiles as well as the abundance jump models at  $\sim 150$ –220 K.

We ran a similar model for the  $\text{H}_2^{18}\text{O}$  lines. The model (presented in Section 4.2.5) with a gradual increase of the abundance at the cold envelope/hot core transition is presented in Figure 9 (green dashed lines). The lines are here again reproduced as well as by the jump abundance models. The HDO/ $\text{H}_2\text{O}$  ratio shows consequently the same variation between the inner and outer regions as found before, i.e.  $5.6 \times 10^{-4}$  at  $T > 200$  K and  $1.3 \times 10^{-3}$  at  $T < 100$  K.

### 4.3 Comparison with previous studies

The singly deuterated form of water has been studied toward many high-mass hot cores with ground-based telescopes (Jacq et al. 1990;

Gensheimer et al. 1996; Pardo et al. 2001; van der Tak et al. 2006). These studies are relevant for the hot core study but do not directly address for the cold external envelope, since the observations of the ground HDO transition at 894 GHz with a very good signal-to-noise ratio are necessary in order to disentangle the contribution from the hot core to the contribution of the cold envelope. The launch of the *Herschel* Space Observatory dramatically changed the situation, with the access to the high frequency range with many HDO transitions available in addition to the ground-state transition. The D/H ratio in water remained for a long time very poorly known since the study of water was based on observations suffering from dilution in the large beams of the Infrared Space Observatory (ISO), the Submillimeter Wave Astronomy Satellite (SWAS) and the ODIN satellite as well as from large opacities. The only way to study water from the ground was to use the  $\text{H}_2^{18}\text{O}$  transition available with some telescopes at 203 GHz (Jacq et al. 1988; van der Tak et al. 2006; Jørgensen & van Dishoeck 2010; Persson et al. 2012, 2013). With the help of this line, the water deuterium fractionation was previously estimated in the high-mass star-forming region G34 by Jacq et al. (1990), Gensheimer et al. (1996), and Liu et al. (2013). They found, in its hot core, HDO/ $\text{H}_2\text{O}$  ratios ranging between  $1 \times 10^{-4}$  and  $4 \times 10^{-4}$ . Since our modeling in the hot core region is mostly dominated by the 81, 226 and 241 GHz transitions accessible from the ground, these values are relatively consistent with our estimate of  $(5-6) \times 10^{-4}$  both with the rotational diagram approach and the non-LTE 1D analysis. Note that we assumed an  $\text{H}_2^{16}\text{O}/\text{H}_2^{18}\text{O}$  ratio of 400, whereas the previous studies assumed 500. In addition, the HDO/ $\text{H}_2\text{O}$  ratio found in this hot core is consistent with the average HDO/ $\text{H}_2\text{O}$  ratio (a few  $10^{-4}$ ) found in other high-mass sources (Jacq et al. 1990; Gensheimer et al. 1996; Pardo et al. 2001; van der Tak et al. 2006; Emprechtinger et al. 2013).

In the hot core, we also determined the water abundance (relative to  $\text{H}_2$ ) to be a few  $\times 10^{-4}$ . Similar values were estimated in other high-mass hot cores (Chavarría et al. 2010; Herpin et al. 2012; Neill et al. 2013), although lower values were also found, for example, in NGC 6334 I ( $\sim 10^{-6}$ , Emprechtinger et al. 2013). The value of  $10^{-4}$  is comparable to the observed abundance of solid water and together with the derived HDO/ $\text{H}_2\text{O}$  abundance ratios of  $10^{-4} - 10^{-3}$  suggests that the origin of the observed water is evaporation of grain mantles.

Recently, Liu et al. (2013) also attempted to constrain the D/H ratio for water in the outer envelope of G34 using the 894 GHz transition observed from the ground with APEX. From a RATRAN modeling using an abundance jump profile at 100 K, they failed to reproduce the profile of this ground state transition leading to a very uncertain value for the D/H ratio in the outer region of the envelope of  $(1.9-4.9) \times 10^{-4}$ . With the sensitivity of *Herschel*/HIFI observations of the 894 GHz transition, it became possible to measure accurately the D/H ratio of water in low-mass (Coutens et al. 2012, 2013) and high-mass protostars, from the hot core region to the cold external envelope. We showed here that, with a value of  $(1.0-2.2) \times 10^{-3}$  in the colder envelope, the HDO/ $\text{H}_2\text{O}$  ratio is indeed higher than the estimate by Liu et al. (2013). It is also higher than in the hot core. A similar behavior was discovered in the low-mass sources IRAS16293 and NGC1333 IRAS4A (Coutens et al. 2013a, 2013b). But this is the first time that a radial variation of the D/H ratio has been observed towards a high-mass star-forming region. The HDO/ $\text{H}_2\text{O}$  ratio derived in the colder envelope of G34 is among the highest values found in high-mass sources. It is close to the high value of  $(2-4) \times 10^{-3}$  found in Orion KL (Persson et al. 2007; Neill et al. 2013) but lower by more than a factor 10 than

in the absorbing layer of low-mass protostars (Coutens et al. 2012, 2013).

## 5 CHEMICAL MODELING

In order to study the chemical pathways that could lead to the observed HDO and  $\text{H}_2\text{O}$  abundances and their corresponding ratio, we modeled the chemical evolution of the source as a function of its radius, using the full gas-grain chemical model Nautilus (Hersant et al. 2009).

### 5.1 Model

Nautilus is a gas grain chemical code adapted from the original code developed by the Herbst group (Hasegawa & Herbst 1993). It solves the kinetic equations of gas-phase chemistry, takes into account grain surface chemistry, and interactions between both phases (adsorption, thermal and non-thermal desorption). The rate equations follow Hasegawa et al. (1992) and Caselli et al. (1998). More details on the processes included in the code are presented by Semenov et al. (2010). The chemical network is adapted from Aikawa et al. (2012) and Furuya et al. (2012). As pointed out by Pagani et al. (1992), Flower et al. (2004, 2006a,b), Walmsley et al. (2004), and Pagani et al. (2009), considering ortho and para spin modifications of various H and D bearing species is important due to some reactions which are much faster with ortho- $\text{H}_2$  than para- $\text{H}_2$ , and can change the entire chemistry of deuterium fractionation. Thus, we extended the network including the ortho, para, and meta states of  $\text{H}_2$ ,  $\text{D}_2$ ,  $\text{H}_3^+$ ,  $\text{H}_2\text{D}^+$ ,  $\text{D}_2\text{H}^+$ , and  $\text{D}_3^+$ . For the reactions involving these species, we have applied spin selection rules to know which reactions are allowed, and have determined branching ratios assuming a total scrambling and a pure nuclear spin statistical weight. Some of the rate coefficients of these reactions have been theoretically or experimentally determined (Marquette et al. 1988; Jensen et al. 2000; McCall et al. 2004; Dos Santos et al. 2007; Hugo et al. 2009; Honvault et al. 2011a,b; Dislaire et al. 2012) and for these we used the calculated or measured values. We have benchmarked our model against some previous work that includes spin-state chemistry, using the same conditions as described in Figure 8 of Pagani et al. (2009) and Figure 4 of Sipilä et al. (2013): a temperature of  $\sim 10$  K and a density from  $\sim 10^5$  to  $\sim 10^6$   $\text{cm}^{-3}$ . Minor differences in abundances do exist, since the networks, the models, and the input parameters can be slightly different, but the result is globally similar. A notable difference is however seen for HD after  $10^5$  yrs as compared with Sipilä et al. (2013). They predict a decrease of its gas phase abundance by one order of magnitude at  $10^6$  yr. Under the same conditions, we predict a decrease in the gas phase HD abundance of only a factor  $\approx 2$ , similar to the model of Albertsson et al. (2013, 2014, priv. com.). The inclusion in our model of photodesorption and reactive desorption may have some effect on HD depletion. Photodesorption due to direct interstellar UV photons and secondary photons generated by cosmic rays, as well as the exothermic association between the surface species H and D, may both release enough HD molecules to the gas phase to lower the HD depletion. The network and a benchmark will be presented in more detail in a forthcoming paper (U. Hincelin et al., in preparation).

In our model, elemental and initial abundances follow Hincelin et al. (2011). Initially, the ortho-to-para  $\text{H}_2$  ratio is set to its statistical value of 3, and deuterium is assumed to be entirely

in HD form with an abundance of  $1.5 \times 10^{-5}$  relative to total hydrogen, following Kong et al. (2013). Note that the timescale for conversion to a thermal ortho-to-para  $H_2$  ratio is a few times  $10^5$  to a few times  $10^6$  yr at 10 K depending on the density, as in Pagani et al. (2009). In the evolutionary sequence of high-mass star formation proposed by Beuther et al. (2007) and Zinnecker & Yorke (2007), infrared dark clouds (IRDCs) are expected to be the first stage. Comparing observations of high-mass star-forming regions with advanced gas-grain chemical modeling, Gerner et al. (2014) derived a chemical age for this stage of around  $10^4$  yrs. The mean density and temperature of IRDCs are respectively  $10^5 \text{ cm}^{-3}$  and 16 K (Sridharan et al. 2005). From the initial elemental and chemical abundances, we have computed the chemical evolution over a period of  $10^4$  yrs, corresponding to  $t_{\text{IRDC}}$  in Figure 10, with a temperature of 16 K, a proton density of  $2 \times 10^5 \text{ cm}^{-3}$ , and a visual extinction of 30. In our standard model, we use a cosmic ray ionization rate of  $1.3 \times 10^{-17} \text{ s}^{-1}$ , but also use a value ten times higher, as discussed in Section 5.2. Following this first phase, we switched to a time-independent one-dimensional physical structure of G34 derived by van der Tak et al. (2013) as seen in Figure B1, and allowed the time-dependent chemistry to continue to evolve independently at each value of the radius of the source.

## 5.2 Results

Figure 10 shows the computed fractional abundances for gaseous HDO and  $H_2O$  relative to the total proton density and their ratio as a function of the radius of the source, at different times following the IRDC stage. The computed values can be compared with the values that best fit the observations, as listed in Table 2. The observational values are given for two points in the table, the inner hot core and the colder envelope, but these values are represented as areas in the figures with their height referring to uncertainty and their length to the length of the inner and outer regions. Note that observational results may not be constant as a function of radius, as shown for the abundances in Sections 4.2.4 and 4.2.5.

During the IRDC phase, water and HDO are present mainly on the grain surfaces, with the water abundance  $\approx 10^{-4}$ . Once we apply the physical profile of the source, the temperature in the inner region, greater than  $\sim 100$  K, is high enough to allow the rapid desorption of  $H_2O$  and HDO, and a transition region is observed around  $6 \times 10^3$  AU, which corresponds to  $\sim 100$  K. Beyond  $6 \times 10^3$  AU, the reverse effect is observed: molecules are slowly adsorbed onto grain surfaces depending on the radius, because the density of the source is now higher than during the IRDC phase. The rate of adsorption is directly proportional to the density, and since the density is higher for small radii, the gaseous molecules are adsorbed more quickly closer to the transition region. This effect is clearly seen at times of  $10^3$  yrs and longer. While the gas-phase water fractional abundance predicted by the chemical model in the inner core (radius  $\leq 5000$  AU) is almost constant, at  $10^{-4}$  to  $10^{-5}$  relative to the total proton density, in the colder envelope, the water abundances lie between a few  $\times 10^{-7}$  and  $10^{-9}$  depending on the radius and the time. This dependence also holds for HDO, which possesses an inner-core abundance between  $10^{-8}$  and  $10^{-9}$ , and an outer abundance between a few  $\times 10^{-9}$  and  $10^{-12}$ .

In addition to these gas-grain interactions, chemical reactions are also occurring. In the inner core, gaseous water is mainly destroyed by reactions with atomic hydrogen:  $H + H_2O \rightarrow OH + \textit{ortho-H}_2$ , and  $H + H_2O \rightarrow OH + \textit{para-H}_2$ . However, water is efficiently reformed by the reverse reactions, so its abundance does not change significantly. In the same region, HDO is also mainly de-

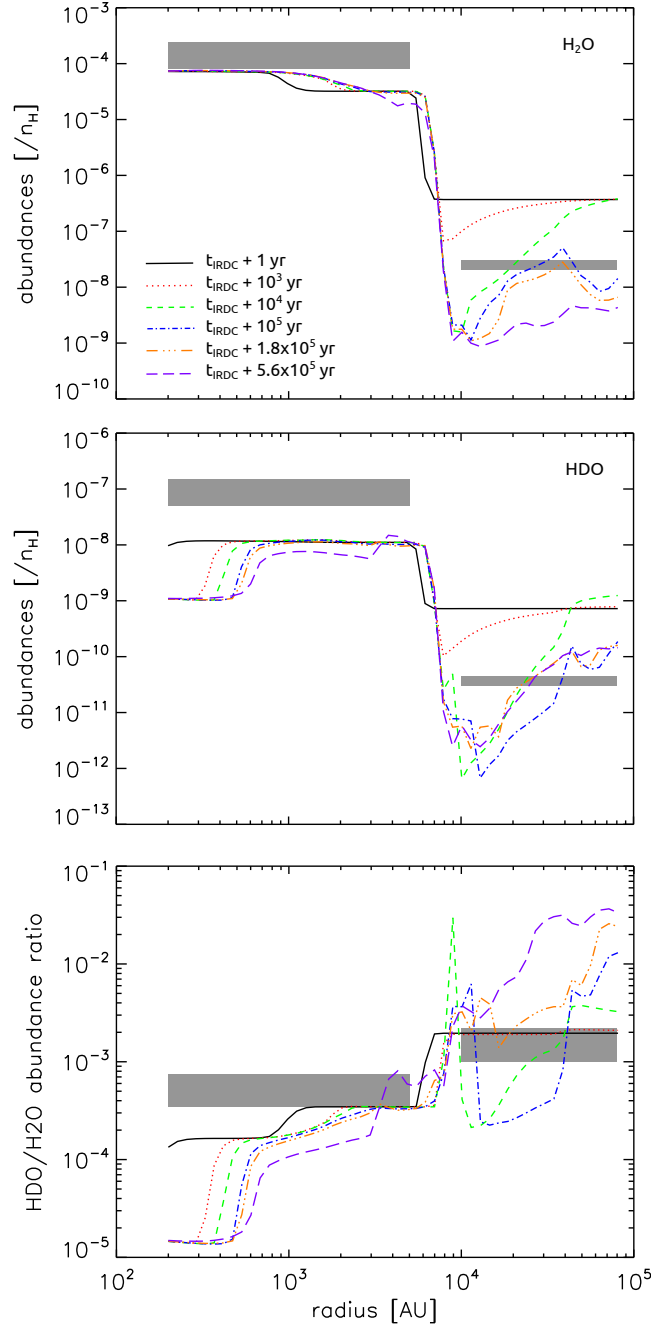


**Figure 10.** Top and center: calculated gas-phase abundances of  $H_2O$  and HDO relative to the total density of protons. Gray areas show observational values and uncertainties of  $H_2O$  and HDO, observed in the hot inner core and the colder envelope. Bottom: HDO/ $H_2O$  gas-phase abundance ratio. Gray areas show observational values and uncertainties of HDO/ $H_2O$  gas-phase abundance ratio observed in the hot inner core and the colder envelope (see Sections 4.2.2 and 4.2.3 for information about uncertainties). Both abundances are plotted as a function of the radius of the source. The results are time dependent, and the colors and types of lines correspond to different values after the first initial phase: black solid lines ( $t = t_{\text{IRDC}} + 1$  yr), red dotted lines ( $t = t_{\text{IRDC}} + 10^3$  yr), green short dashed lines ( $t = t_{\text{IRDC}} + 10^4$  yr), blue dashed dotted (1 dot) lines ( $t = t_{\text{IRDC}} + 10^5$  yr), orange dashed dotted (3 dots) lines ( $t = t_{\text{IRDC}} + 1.8 \times 10^5$  yr), and purple long dashed lines ( $t = t_{\text{IRDC}} + 5.6 \times 10^5$  yr). (A color version of this figure is available in the online journal.)

stroyed by reactions with atomic hydrogen:  $\text{H} + \text{HDO} \rightarrow \text{OH} + \text{HD}$ ,  $\text{H} + \text{HDO} \rightarrow \text{OD} + \text{ortho-H}_2$ , and  $\text{H} + \text{HDO} \rightarrow \text{OD} + \text{para-H}_2$ . Although HDO is also reformed by the reverse reactions, these processes are sufficiently slower than the destruction reactions that the HDO abundance decreases, with an efficiency depending on the local temperature. This is indicated by the dashed lines in the upper panel of Figure 10, particularly within a radius of 1000 AU. Thus, we observe a general decrease of the  $\text{HDO}/\text{H}_2\text{O}$  ratio in the hot inner core as a function of time.

In the colder envelope, at larger radii, the  $\text{H}_2\text{O}$  gas phase abundance is reduced due to adsorption, as discussed above, and ion-molecule reactions, particularly the reaction with  $\text{HCO}^+$ , which forms  $\text{H}_3\text{O}^+$  and CO. Before  $t = t_{\text{IRDC}} + 10^4$  yrs,  $\text{HCO}^+$  mainly reacts with carbon atoms, and after this time, the carbon atom abundance is low enough to allow an increase of the  $\text{HCO}^+$  abundance through ion-molecule reactions involving CO. Although HDO also reacts with  $\text{HCO}^+$ , it is partially reformed by ion-molecule reactions involving  $\text{H}_2\text{DO}^+$ , and dissociative recombination of  $\text{H}_2\text{DO}^+$  with an electron.  $\text{H}_2\text{O}$  is also reformed by reactions involving  $\text{H}_3\text{O}^+$ , but not as efficiently as HDO. At later times, the abundances of  $\text{HDO}^+$  and  $\text{H}_2\text{DO}^+$  are increased, while the ones of  $\text{H}_2\text{O}^+$  and  $\text{H}_3\text{O}^+$  are decreased, so that the  $\text{HDO}/\text{H}_2\text{O}$  abundance ratio increases.

At  $10^4$  AU, next to the transition region, the temperature and density are respectively equal to 80 K and  $10^6 \text{ cm}^{-3}$ . Here, there is a complex competition between the formation of HDO and  $\text{H}_2\text{O}$  in the gas phase and the adsorption and desorption of these molecules. For this reason, we get temporarily a peak in the  $\text{HDO}/\text{H}_2\text{O}$  ratio around  $10^4$  and  $10^5$  yrs (respectively the green and blue peak). The main gas phase reactions involved are the following:  $\text{H}_3\text{O}^+$  and  $\text{H}_2\text{DO}^+$  react with DCN, DNC, HCN, and HNC, which form HDO and  $\text{H}_2\text{O}$ . Besides, after  $10^4$  yrs,  $\text{H}_2\text{CO}$  plays also a role: it is slowly released from the grain surface, and reacts efficiently with OH and OD to form respectively  $\text{H}_2\text{O}$  and HDO. However, at this temperature and density, adsorption of HDO and  $\text{H}_2\text{O}$  is still quite efficient, and removes a part of these molecules from the gas phase.

If we compare the computed abundances of water and HDO with the observational values, seen as gray areas in Figure 10, the  $\text{H}_2\text{O}$  abundances are in good agreement in both the hot inner core and the colder outer envelope. This also holds true for HDO in the colder envelope; however, our model does not produce enough HDO in the hot inner core at all times. Specifically, our values are five to fifty times less than those indicated by the observations, depending on the time and the radius. Given the low abundance of HDO in the hot inner core, our calculated gaseous  $\text{HDO}/\text{H}_2\text{O}$  ratio is lower than the observed one throughout this region, while in the colder outer envelope, our ratio lies within the range of the observational values at selected times. Note that the observational abundances and ratio may not be constant as a function of radius in the two regions, so more constraints are necessary to compare with the model results.

The HDO abundance profiles in the cold outer region from Figure 10 favor the best-fit abundance profile for water from Figure 7, which increases with radius in the cold envelope. A comparison between the HDO profiles of these two figures leads to the best agreement around  $t = t_{\text{IRDC}} + 10^5$  yrs. This time corresponds to the best-fit chemical age of Gerner et al. (2014): their high mass protostellar object stage, the stage just after the IRDC stage, lasts  $\sim 6 \times 10^4$  yrs, and the following stage, the hot molecular core stage, lasts  $\sim 4 \times 10^4$  yrs, which give a total similar to ours.

We have tested the sensitivity of  $\text{H}_2\text{O}$  and HDO to the cosmic-ray ionization rate, using a value of  $1.3 \times 10^{-16} \text{ s}^{-1}$ , which is ten

times higher than the standard rate. This value is close to the upper limit derived in this source (see Section 4.2.4). Cosmic rays are the main source of ions in clouds, and formation and destruction of neutral species involve mainly reactions with charged species. As a consequence, most of the molecules are sensitive to the cosmic-ray ionization rate (Wakelam et al. 2010). Compared with our standard model, in the cold envelope, the gas phase  $\text{H}_2\text{O}$  abundance is decreased by one order of magnitude at early times after the IRDC phase. Then,  $\text{H}_2\text{O}$  is reformed quite efficiently so that the final abundance is one order of magnitude higher than with our standard model. In the same region, the HDO abundance is increased by a factor 10 to 100 depending on the time. The  $\text{HDO}/\text{H}_2\text{O}$  ratio is then enhanced, and higher than the observational value by a factor of  $\sim 100$  and  $< 2$  respectively at early and later times. In the inner core, the  $\text{H}_2\text{O}$  abundance is slightly increased to a value  $\geq 10^{-4}$  at all times. The HDO abundance is more sensitive at early times to the cosmic ionization rate: it is firstly increased by a factor of 100, but then the value tends to decrease to the same one as in our standard model. The  $\text{HDO}/\text{H}_2\text{O}$  ratio is also enhanced, up to a factor of 100 at early times, but tends to decrease to the same value as in our standard model. In the IRDC phase and the cold envelope, gaseous  $\text{H}_2\text{O}$  is mainly formed by reactions involving  $\text{H}_3\text{O}^+$  and destroyed by reactions with  $\text{HCO}^+$  and  $\text{C}^+$ , while  $\text{H}_2\text{DO}^+$  is the main reactant involved in the formation of HDO. In the inner hot core, the abundances of  $\text{H}_2\text{O}$  and HDO are mainly changed due to OH and OD which are sensitive to the cosmic ray ionization rate (Wakelam et al. 2010).

We have also tested the sensitivity of our modeling to the inclusion of spin-state chemistry, and provide in Appendix C the results of a simulation using our chemical network without considering the spin states. Our main conclusion is that the gas phase HDO abundance is not only sensitive to the inclusion of spin-state chemistry at low temperature, but also at high temperature, although the difference is less strong. In addition, the  $\text{H}_2\text{O}$  abundance is slightly sensitive at longer times to the spin-state chemistry in the cold envelope region, but not in the hot inner core region. The overall ratio  $\text{HDO}/\text{H}_2\text{O}$  decreases if we take into account spin state chemistry, as it can be predicted based simply on the thermodynamics of protonated ion-HD exchange reactions.

### 5.3 Comparison with other studies

Below we compare our results for water and HDO both in the gas and on ice mantles with those of earlier studies. We first consider ice mantles. Some of these studies include spin-state chemistry while others do not.

Several groups theoretically studied deuteration of water in star forming regions (i.e. Cazaux et al. 2011; Aikawa et al. 2012; Sipilä et al. 2013; Taquet et al. 2013, 2014). These studies focus on low mass star-formation regions or cold conditions, and as a consequence generally deal with lower temperatures and densities than ours. However, considering the external region of the cold envelope of our source, where the conditions are the closest to these studies ( $30 \text{ K}$  and  $10^5 \text{ cm}^{-3}$ ), it is worth making some comparisons with our ice results. Our  $\text{HDO}/\text{H}_2\text{O}$  ice ratio in the cold envelope varies between  $10^{-4}$  and  $10^{-3}$  depending on the time. The larger the time, the larger the ratio. We can compare our values to those in Figures 11 and 12 in Sipilä et al. (2013) and Figure 8 in Taquet et al. (2013). These studies also include spin state chemistry. In general, we predict a lower  $\text{HDO}/\text{H}_2\text{O}$  ice ratio than these studies. Despite our slightly higher temperature, and multiple differences between our models, the initial ortho-to-para  $\text{H}_2$  ratio may be the

main reason, since a higher value tends to decrease the deuterium fractionation. Cazaux et al. (2011) and Aikawa et al. (2012), who did not consider the spin state chemistry, predicted an HDO/H<sub>2</sub>O ice ratio of  $\sim 0.01$ , which then can be considered as an upper limit.

Aikawa et al. (2012) and Taquet et al. (2014) studied the deuteration of molecules as a function of the radius of a forming protostellar core. Here we can compare calculated HDO/H<sub>2</sub>O ratios in the gas phase. Their temperature and density gradient along the radius is quite important, from  $\sim 10$  K and  $\sim 10^4$  cm<sup>-3</sup> to several hundred Kelvin and  $10^{12}$  cm<sup>-3</sup>, close to the range of conditions of our source. Note that these studies include a dynamical physical structure instead of a static structure. Despite the differences between our model and these earlier studies, we obtain the same qualitative pattern, in which the gas phase water abundance is higher in the inner and hot region, while it is lower in the outer and cold region. In the outer region, the abundance is governed mainly by the density, and as a consequence, tends to be lower when the density gets higher. Their HDO/H<sub>2</sub>O ratio changes by one to two orders of magnitude between the cold region and the hot region, and is higher in the colder region.

## 6 CONCLUSIONS

Ten lines of HDO and three lines of H<sub>2</sub><sup>18</sup>O covering a broad range of upper energy levels (22–204 K) were detected with the *Herschel*/HIFI instrument, the IRAM-30m telescope, and the CSO towards the high-mass star-forming region G34.26+0.15. Using a 1D non-LTE radiative transfer code, we constrained the abundance distribution of HDO and H<sub>2</sub><sup>18</sup>O throughout the envelope from the hot core to the colder regions. To reproduce the HDO line profiles, it is necessary to assume an abundance jump at a temperature higher than 100 K ( $\sim 150$ –220 K), which suggests that the hot core is smaller than expected. This could be explained by the fact that the water abundance increases gradually within a certain temperature range between the cold envelope and the hot core, as suggested by some chemical models considering dynamics (Aikawa et al. 2012, Wakelam et al. submitted). Another explanation would be that the structure is relatively uncertain at small scales. Similar studies (including observations of the HDO lines at 226 and 242 GHz, as well as some HIFI lines at 491, 600, or 919 GHz) should be carried out towards other high-mass sources to know if this higher jump temperature is specific to G34 or common to other objects. Using different types of water abundance profiles, we showed that the water deuterium fractionation in the hot core and in the colder envelope is strongly constrained. Assuming calibration uncertainties of 20%, the HDO/H<sub>2</sub>O ratio is estimated to be about  $(3.5\text{--}7.5) \times 10^{-4}$  in the hot core. It is in agreement with the value derived with the rotational diagram analysis of the IRAM-30m lines as well as with previous studies (Jacq et al. 1990; Liu et al. 2013). In the colder gas, we determined the HDO/H<sub>2</sub>O ratio to be about  $(1.0\text{--}2.2) \times 10^{-3}$ , including the uncertainties. Although radial variations of the water deuterium fractionation have already been observed in low-mass protostars (Coutens et al. 2012, 2013a, 2013b), this is the first time that a decrease of the water deuterium fractionation in the warmer regions has been measured in a high-mass star-forming region. Finally, we modeled the chemical evolution of G34 as a function of its radius and showed that our model reproduces relatively well the observational results that assumed an increase of the water abundance with radius in the cold regions (see Figures 7 and 10). The comparison of the chemical model and the observations favors an

age of  $10^5$  years after the IRDC stage, which is consistent with the age derived for hot molecular cores by Gerner et al. (2014).

## ACKNOWLEDGMENTS

The authors are grateful to the anonymous referee for his/her useful and pertinent comments and suggestions. They thank K. Furuya and Y. Aikawa for providing the initial chemical network of deuterated species and N. Flagey for providing the reduced HIFI data of H<sub>2</sub><sup>18</sup>O. They would also like to thank M. Hajigholi for fruitful discussions regarding the source modeling. A. C. and C. V. thank PCMI for support of the *Herschel* HIFI project on deuterated water. C. M. P. acknowledges generous support from the Swedish National Space Board. Support for this work was also provided by NASA through an award issued by JPL/Caltech.

This work is based on observations carried out with the HIFI instrument onboard the *Herschel Space Observatory*, the Institut de RadioAstronomie Millimétrique (IRAM) 30m Telescope and the Caltech Submillimeter Telescope (CSO). *Herschel* is an ESA space observatory with science instruments provided by European-led principal Investigator consortia and with important participation from NASA. HIFI has been designed and built by a consortium of institutes and university departments from across Europe, Canada and the United States under the leadership of SRON Netherlands Institute for Space Research, Groningen, The Netherlands and with major contributions from Germany, France and the US. Consortium members are: Canada: CSA, U. Waterloo; France: IRAP (formerly CESR), LAB, LERMA, IRAM; Germany: KOSMA, MPIfR, MPS; Ireland, NUI Maynooth; Italy: ASI, IFSI-INAF, Osservatorio Astrofisico di Arcetri-INAF; Netherlands: SRON, TUD; Poland: CAMK, CBK; Spain: Observatorio Astronómico Nacional (IGN), Centro de Astrobiología (CSIC-INTA). Sweden: Chalmers University of Technology - MC2, RSS & GARD; Onsala Space Observatory; Swedish National Space Board, Stockholm University - Stockholm Observatory; Switzerland: ETH Zurich, FHNW; USA: Caltech, JPL, NHSC. IRAM is supported by INSU/CNRS (France), MPG (Germany) and IGN (Spain). The CSO is operated by the California Institute of Technology under cooperative agreement with the National Science Foundation (AST-0838261).

## REFERENCES

- Aikawa Y., Wakelam V., Hersant F., Garrod R. T., Herbst E., 2012, *ApJ*, 760, 40
- Albertsson T., Indriolo N., Kreckel H., Semenov D., Crabtree K. N., Henning T., 2014, *ApJ*, 787, 44
- Albertsson T., Semenov D. A., Vasyunin A. I., Henning T., Herbst E., 2013, *ApJS*, 207, 27
- Alexander C. M. O. D., Bowden R., Fogel M. L., Howard K. T., Herd C. D. K., Nittler L. R., 2012, *Science*, 337, 721
- Bergin E. A., Neufeld D. A., Melnick G. J., 1999, *ApJL*, 510, L145
- Beuther H., Churchwell E. B., McKee C. F., Tan J. C., 2007, *Protostars and Planets V*, pp 165–180
- Bockelée-Morvan D., Biver N., Swinyard B., de Val-Borro M., Crovisier J., Hartogh P., Lis D. C., Moreno R., Szutowicz S., Lellouch E., Emprechtinger M., Blake G. A., Courtin R., et al. 2012, *A&A*, 544, L15



- Bockelée-Morvan D., Gautier D., Lis D. C., Young K., Keene J., Phillips T., Owen T., Crovisier J., Goldsmith P. F., Bergin E. A., Despois D., Wootten A., 1998, *Icarus*, 133, 147
- Campins H., Hargrove K., Pinilla-Alonso N., Howell E. S., Kelley M. S., Licandro J., Mothé-Diniz T., Fernández Y., Ziffer J., 2010, *Nature*, 464, 1320
- Caselli P., Hasegawa T. I., Herbst E., 1998, *ApJ*, 495, 309
- Caselli P., Keto E., Bergin E. A., Tafalla M., Aikawa Y., Douglas T., Pagani L., Yıldız U. A., van der Tak F. F. S., Walmsley C. M., Codella C., Nisini B., Kristensen L. E., van Dishoeck E. F., 2012, *ApJL*, 759, L37
- Caselli P., Myers P. C., 1995, *ApJ*, 446, 665
- Cazaux S., Caselli P., Spaans M., 2011, *ApJL*, 741, L34
- Ceccarelli C., Castets A., Caux E., Hollenbach D., Loinard L., Molinari S., Tielens A. G. G. M., 2000, *A&A*, 355, 1129
- Chavarría L., Herpin F., Jacq T., Braine J., Bontemps S., Baudry A., Marseille M., van der Tak F., et al. 2010, *A&A*, 521, L37
- Comito C., Schilke P., Rolfs R., Lis D. C., Belloche A., Bergin E. A., Phillips T. G., Bell T. A., Crockett N. R., et al. 2010, *A&A*, 521, L38+
- Coutens A., Vastel C., Cabrit S., Codella C., Kristensen L. E., Ceccarelli C., van Dishoeck E. F., Boogert A. C. A., Bottinelli S., Castets A., et al. 2013, *A&A*, 560, A39
- Coutens A., Vastel C., Caux E., Ceccarelli C., Bottinelli S., Wiesenfeld L., Faure A., Scribano Y., Kahane C., 2012, *A&A*, 539, A132
- Coutens A., Vastel C., Cazaux S., Bottinelli S., Caux E., Ceccarelli C., Demyk K., Taquet V., Wakelam V., 2013, *A&A*, 553, A75
- Daniel F., Dubernet M.-L., Grosjean A., 2011, *A&A*, 536, A76
- De Buizer J. M., Radomski J. T., Telesco C. M., Piña R. K., 2003, *ApJ*, 598, 1127
- de Graauw T., Helmich F. P., Phillips T. G., Stutzki J., Caux E., Whyborn N. D., Dieleman P., Roelfsema P. R., Aarts H., Assendorp R., Bachiller R., Baechtold W., et al. 2010, *A&A*, 518, L6+
- Dislaire V., Hily-Blant P., Faure A., Maret S., Bacmann A., Pineau Des Forêts G., 2012, *A&A*, 537, A20
- Dos Santos S. F., Kokoouline V., Greene C. H., 2007, *J. Chem. Phys.*, 127, 124309
- Dulieu F., Amiaud L., Congiu E., Fillion J.-H., Matar E., Momeni A., Pirronello V., Lemaire J. L., 2010, *A&A*, 512, A30+
- Emprechtinger M., Lis D. C., Rolfs R., Schilke P., Monje R. R., Comito C., Ceccarelli C., Neufeld D. A., van der Tak F. F. S., 2013, *ApJ*, 765, 61
- Faure A., Wiesenfeld L., Scribano Y., Ceccarelli C., 2011, *MNRAS*, p. 2015
- Flagey N., Goldsmith P. F., Lis D. C., Gerin M., Neufeld D., Sonnentrucker P., De Luca M., Godard B., Goicoechea J. R., Monje R., Phillips T. G., 2013, *ApJ*, 762, 11
- Flower D. R., Pineau des Forêts G., Walmsley C. M., 2004, *A&A*, 427, 887
- Flower D. R., Pineau Des Forêts G., Walmsley C. M., 2006a, *A&A*, 456, 215
- Flower D. R., Pineau Des Forêts G., Walmsley C. M., 2006b, *A&A*, 449, 621
- Fraser H. J., Collings M. P., McCoustra M. R. S., Williams D. A., 2001, *MNRAS*, 327, 1165
- Furuya K., Aikawa Y., Tomida K., Matsumoto T., Saigo K., Tomisaka K., Hersant F., Wakelam V., 2012, *ApJ*, 758, 86
- Garay G., Reid M. J., Moran J. M., 1985, *ApJ*, 289, 681
- Garay G., Rodriguez L. F., van Gorkom J. H., 1986, *ApJ*, 309, 553
- Gaume R. A., Fey A. L., Claussen M. J., 1994, *ApJ*, 432, 648
- Gensheimer P. D., Mauersberger R., Wilson T. L., 1996, *A&A*, 314, 281
- Gerin M., de Luca M., Goicoechea J. R., Herbst E., Falgarone E., Godard B., Bell T. A., Coutens A., Kaźmierczak M., Sonnentrucker P., Black J. H., et al. 2010, *A&A*, 521, L16
- Gerner T., Beuther H., Semenov D., Linz H., Vasyunina T., Bihr S., Shirley Y. L., Henning T., 2014, *A&A*, 563, A97
- Goldsmith P. F., Langer W. D., 1999, *ApJ*, 517, 209
- Hartogh P., Lis D. C., Bockelée-Morvan D., de Val-Borro M., Biver N., Küppers M., Emprechtinger M., Bergin E. A., Crovisier J., Rengel M., Moreno R., Szutowicz S., Blake G. A., 2011, *Nature*, 478, 218
- Hasegawa T. I., Herbst E., 1993, *MNRAS*, 261, 83
- Hasegawa T. I., Herbst E., Leung C. M., 1992, *ApJS*, 82, 167
- Hatchell J., Fuller G. A., Millar T. J., 2001, *A&A*, 372, 281
- Hatchell J., Thompson M. A., Millar T. J., MacDonald G. H., 1998, *A&AS*, 133, 29
- Herpin F., Chavarría L., van der Tak F., Wyrowski F., van Dishoeck E. F., Jacq T., Braine J., Baudry A., Bontemps S., Kristensen L., 2012, *A&A*, 542, A76
- Hersant F., Wakelam V., Dutrey A., Guilloteau S., Herbst E., 2009, *A&A*, 493, L49
- Hincelin U., Wakelam V., Hersant F., Guilloteau S., Loison J. C., Honvault P., Troe J., 2011, *A&A*, 530, A61
- Hogerheijde M. R., Bergin E. A., Brinch C., Cleeves L. I., Fogel J. K. J., Blake G. A., Dominik C., Lis D. C., Melnick G., Neufeld D., Panić O., Pearson J. C., Kristensen L., Yıldız U. A., van Dishoeck E. F., 2011, *Science*, 334, 338
- Hogerheijde M. R., van der Tak F. F. S., 2000, *A&A*, 362, 697
- Hollenbach D., Kaufman M. J., Bergin E. A., Melnick G. J., 2009, *ApJ*, 690, 1497
- Honvault P., Jorfi M., González-Lezana T., Faure A., Pagani L., 2011a, *Physical Review Letters*, 107, 023201
- Honvault P., Jorfi M., González-Lezana T., Faure A., Pagani L., 2011b, *Physical Chemistry Chemical Physics (Incorporating Faraday Transactions)*, 13, 19089
- Hugo E., Asvany O., Schlemmer S., 2009, *J. Chem. Phys.*, 130, 164302
- Ioppolo S., Cuppen H. M., Romanzin C., van Dishoeck E. F., Linnartz H., 2008, *ApJ*, 686, 1474
- Jacq T., Henkel C., Walmsley C. M., Jewell P. R., Baudry A., 1988, *A&A*, 199, L5
- Jacq T., Walmsley C. M., Henkel C., Baudry A., Mauersberger R., Jewell P. R., 1990, *A&A*, 228, 447
- Jensen M. J., Bilodeau R. C., Safvan C. P., Seiersen K., Andersen L. H., Pedersen H. B., Heber O., 2000, *ApJ*, 543, 764
- Jørgensen J. K., van Dishoeck E. F., 2010, *ApJL*, 710, L72
- Kong S., Caselli P., Tan J. C., Wakelam V., 2013, *ArXiv* 1312.0971
- Kristensen L. E., van Dishoeck E. F., Bergin E. A., Visser R., Yıldız U. A., San Jose-Garcia I., Jørgensen J. K., Herczeg G. J., Johnstone D., Wampfler S. F., et al. 2012, *A&A*, 542, A8
- Kristensen L. E., Visser R., van Dishoeck E. F., Yıldız U. A., Doty S. D., Herczeg G. J., Liu F.-C., Parise B., Jørgensen J. K., et al. 2010, *A&A*, 521, L30+
- Kuchar T. A., Bania T. M., 1994, *ApJ*, 436, 117
- Küppers M., O'Rourke L., Bockelée-Morvan D., Zakharov V., Lee S., von Allmen P., Carry B., Teyssier D., Marston A., Müller T., Crovisier J., Barucci M. A., Moreno R., 2014, *Nature*, 505, 525
- Lis D. C., Biver N., Bockelée-Morvan D., Hartogh P., Bergin

- E. A., Blake G. A., Crovisier J., de Val-Borro M., Jehin E., Küppers M., Manfroid J., Moreno R., Rengel M., Szutowicz S., 2013, *ApJL*, 774, L3
- Lis D. C., Phillips T. G., Goldsmith P. F., Neufeld D. A., Herbst E., Comito C., Schilke P., Müller H. S. P., Bergin E. A., Gerin M., Bell T. A., Emprechtinger M., et al. 2010, *A&A*, 521, L26
- Liu F., Parise B., Kristensen L., Visser R., van Dishoeck E. F., Güsten R., 2011, *A&A*, 527, A19+
- Liu F.-C., Parise B., Wyrowski F., Zhang Q., Güsten R., 2013, *A&A*, 550, A37
- Liu T., Wu Y., Zhang H., 2013, *ApJ*, 776, 29
- MacDonald G. H., Gibb A. G., Habing R. J., Millar T. J., 1996, *A&AS*, 119, 333
- Marquette J. B., Rebrion C., Rowe B. R., 1988, *J. Chem. Phys.*, 89, 2041
- McCall B. J., Huneycutt A. J., Saykally R. J., Djuric N., Dunn G. H., Semaniak J., Novotny O., Al-Khalili A., Ehlerding A., Hellberg F., Kalhori S., Neau A., Thomas R. D., Paal A., Österdahl F., Larsson M., 2004, *Phys. Rev. A*, 70, 052716
- Miyauchi N., Hidaka H., Chigai T., Nagaoka A., Watanabe N., Kouchi A., 2008, *Chemical Physics Letters*, 456, 27
- Mokrane H., Chaabouni H., Accolla M., Congiu E., Dulieu F., Chehrouri M., Lemaire J. L., 2009, *ApJL*, 705, L195
- Mookerjee B., Casper E., Mundy L. G., Looney L. W., 2007, *ApJ*, 659, 447
- Mottram J. C., van Dishoeck E. F., Schmalzl M., Kristensen L. E., Visser R., Hogerheijde M. R., Bruderer S., 2013, *A&A*, 558, A126
- Müller H. S. P., Coutens A., Walters A., Grabow J.-U., Schlemmer S., 2011, *Journal of Molecular Spectroscopy*, 267, 100
- Müller H. S. P., Schlöder F., Stutzki J., Winnewisser G., 2005, *Journal of Molecular Structure*, 742, 215
- Neill J. L., Wang S., Bergin E. A., Crockett N. R., Favre C., Plume R., Melnick G. J., 2013, *ApJ*, 770, 142
- Oba Y., Miyauchi N., Hidaka H., Chigai T., Watanabe N., Kouchi A., 2009, *ApJ*, 701, 464
- Öberg K. I., Linnartz H., Visser R., van Dishoeck E. F., 2009, *ApJ*, 693, 1209
- Ossenkopf V., Henning T., 1994, *A&A*, 291, 943
- Ott S., 2010, in *Astronomical Data Analysis Software and Systems XIX Vol. 434 of Astronomical Society of the Pacific Conference Series, The Herschel Data Processing System HIPE and Pipelines Up and Running Since the Start of the Mission.* p. 139
- Pagani L., Salez M., Wannier P. G., 1992, *A&A*, 258, 479
- Pagani L., Vastel C., Hugo E., Kokouline V., Greene C. H., Bacmann A., Bayet E., Ceccarelli C., Peng R., Schlemmer S., 2009, *A&A*, 494, 623
- Pardo J. R., Cernicharo J., Herpin F., Kawamura J., Kooi J., Phillips T. G., 2001, *ApJ*, 562, 799
- Parise B., Caux E., Castets A., Ceccarelli C., Loinard L., Tielens A. G. G. M., Bacmann A., Cazaux S., Comito C., Helmich F., Kahane C., Schilke P., van Dishoeck E., Wakelam V., Walters A., 2005, *A&A*, 431, 547
- Persson C. M., Olofsson A. O. H., Koning N., Bergman P., Bernath P., Black J. H., Frisk U., Geppert W., Hasegawa T. I., Hjalmarsen Å., Kwok S., Larsson B., Lecacheux A., Nummelin A., Olberg M., Sandqvist A., Wiström E. S., 2007, *A&A*, 476, 807
- Persson M. V., Jørgensen J. K., van Dishoeck E. F., 2012, *A&A*, 541, A39
- Persson M. V., Jørgensen J. K., van Dishoeck E. F., 2013, *A&A*, 549, L3
- Persson M. V., Jørgensen J. K., van Dishoeck E. F., Harsono D., 2014, *A&A*, 563, A74
- Pickett H. M., Poynter R. L., Cohen E. A., Delitsky M. L., Pearson J. C., Müller H. S. P., 1998, *J. Quant. Spec. Radiat. Transf.*, 60, 883
- Pilbratt G. L., Riedinger J. R., Passvogel T., Crone G., Doyle D., Gageur U., Heras A. M., Jewell C., Metcalfe L., Ott S., Schmidt M., 2010, *A&A*, 518, L1+
- Prasad S. S., Tarafdar S. P., 1983, *ApJ*, 267, 603
- Reid M. J., Ho P. T. P., 1985, *ApJL*, 288, L17
- Roberts H., Herbst E., 2002, *A&A*, 395, 233
- Roelfsema P. R., Helmich F. P., Teyssier D., Ossenkopf V., Morris P., Olberg M., Shipman R., Risacher C., Akyilmaz M., Asendorp R., Avruch I. M., Beintema D., Biver N., Boogert A., Borys C., Braine J., et al. 2012, *A&A*, 537, A17
- Rolfs R., Schilke P., Comito C., Bergin E. A., van der Tak F. F. S., Lis D. C., Qin S.-L., Menten K. M., Güsten R., et al. 2010, *A&A*, 521, L46
- Semenov D., Hersant F., Wakelam V., Dutrey A., Chapillon E., Guilloteau S., Henning T., Launhardt R., Piétu V., Schreyer K., 2010, *A&A*, 522, A42
- Sewilo M., Churchwell E., Kurtz S., Goss W. M., Hofner P., 2004, *ApJ*, 605, 285
- Sewilo M., Churchwell E., Kurtz S., Goss W. M., Hofner P., 2011, *ApJS*, 194, 44
- Shen C. J., Greenberg J. M., Schutte W. A., van Dishoeck E. F., 2004, *A&A*, 415, 203
- Sipilä O., Caselli P., Harju J., 2013, *A&A*, 554, A92
- Sridharan T. K., Beuther H., Saito M., Wyrowski F., Schilke P., 2005, *ApJL*, 634, L57
- Taquet V., Charnley S. B., Sipilä O., 2014, *ApJ*, 791, 1
- Taquet V., Peters P. S., Kahane C., Ceccarelli C., López-Sepulcre A., Toubin C., Dufort D., Wiesenfeld L., 2013, *A&A*, 550, A127
- Tielens A. G. G. M., Hagen W., 1982, *A&A*, 114, 245
- Turner B. E., Balick B., Cudaback D. D., Heiles C., Boyle R. J., 1974, *ApJ*, 194, 279
- van der Tak F. F. S., Chavarría L., Herpin F., Wyrowski F., Walmsley C. M., van Dishoeck E. F., Benz A. O., Bergin E. A., Caselli P., Hogerheijde M. R., Johnstone D., Kristensen L. E., Liseau R., Nisini B., Tafalla M., 2013, *A&A*, 554, A83
- van der Tak F. F. S., Walmsley C. M., Herpin F., Ceccarelli C., 2006, *A&A*, 447, 1011
- van Dishoeck E. F., Herbst E., Neufeld D. A., 2013, *Chemical Reviews*, 113, 9043
- Wakelam V., Herbst E., Le Boulrot J., Hersant F., Selsis F., Guilloteau S., 2010, *A&A*, 517, A21
- Walmsley C. M., Flower D. R., Pineau des Forêts G., 2004, *A&A*, 418, 1035
- Watanabe N., Kouchi A., 2008, *Progress In Surface Science*, 83, 439
- Watt S., Mundy L. G., 1999, *ApJS*, 125, 143
- Wilson T. L., 1999, *Reports on Progress in Physics*, 62, 143
- Wood D. O. S., Churchwell E., 1989, *ApJS*, 69, 831
- Wyrowski F., Güsten R., Menten K. M., Wiesemeyer H., Klein B., 2012, *A&A*, 542, L15
- Zinnecker H., Yorke H. W., 2007, *ARA&A*, 45, 481

**APPENDIX A: *HERSCHEL*/HIFI OBSERVATIONS**

The observing IDs of the *Herschel*/HIFI data are listed in Table A1.

**APPENDIX B: NON-LTE SPHERICAL RADIATIVE TRANSFER MODELING****B1 Density and temperature profiles**

The density and temperature profiles used for the model of the HDO and  $\text{H}_2^{18}\text{O}$  lines are shown in Figure B1.

**B2 Velocity field profiles**

The radial velocity profile ( $v_r$ ) and the turbulence width (Doppler b-parameter,  $db$ ) are required inputs for the RATRAN radiative transfer modeling. We do not have direct information on them, except that inward motions are necessary to reproduce the inverse P-Cygni profile observed on the HDO  $1_{1,1}-1_{0,0}$  fundamental line observed with HIFI. Indeed, with a static envelope, the model predicts an absorbing component at the local standard velocity of rest,  $V_{\text{LSR}} = 58 \text{ km s}^{-1}$ , whereas the absorption is observed at  $61 \text{ km s}^{-1}$  only. Consequently, it is not possible to reproduce the line profile of this HDO fundamental transition with a static envelope and an unrelated absorbing layer situated on the line of sight. The radial velocity was then fixed at  $-3 \text{ km s}^{-1}$  in the cold outer regions.

To estimate the  $v_r$  and  $db$  profiles throughout the envelope, we assumed abundance profiles with a jump and proceeded as follows: *i*) First, we assume an initial profile for the radial velocity and the Doppler b-parameter. Then we run a grid of models with various inner ( $T > T_j$ ) and outer ( $T < T_j$ ) abundances. *ii*) If the predicted line profiles do not fit at all the data, we choose the model that gives the best agreement with respect to the intensities. Keeping the same abundances as this model, we modify the velocity profiles to obtain better agreement. *iii*) Then we run another grid of models with these new velocity profiles and go back to step (*ii*) if necessary and so on.

Models with infall profiles were attempted but, as shown in Figure B3, some of the HDO lines (509, 600, 849, and 919 GHz) are shifted in velocity with respect to the observations when this type of profile is taken into account. On the contrary, models with outward motions in the inner regions give a good agreement for the different HDO lines. These outward motions could be produced by stellar winds or outflows.

To limit the number of free parameters in the study, we only considered constant  $v_r$  and  $db$  values in the inner and outer regions. Based on the widths of the different lines, the  $v_r$  parameter was determined to be about  $4 \text{ km s}^{-1}$  in the inner regions in expansion and about  $-3 \text{ km s}^{-1}$  in the infalling outer regions. The Doppler b-parameter is estimated to be about  $2.5 \text{ km s}^{-1}$  in the outer region. This constraint is based on the width of the absorption component of the HDO line at 894 GHz. In the inner regions, the fit of the emission lines is slightly better with  $db \sim 2.0 \text{ km s}^{-1}$ . The  $db$  parameter seems to decrease from the outer to the inner regions, similarly to other studies in high mass sources (Caselli & Myers 1995; Herpin et al. 2012). To be able to reproduce the HDO and  $\text{H}_2^{18}\text{O}$  lines with a unique velocity profile for all the models with different jump temperatures, we delimited the change of the  $db$  and  $v_r$  values between the inner and outer region at 100 K. The final velocity fields used in the paper are presented in Figure B2. We cannot however exclude that different velocity fields (possibly more complex) would reproduce the lines. For the models assuming an increase

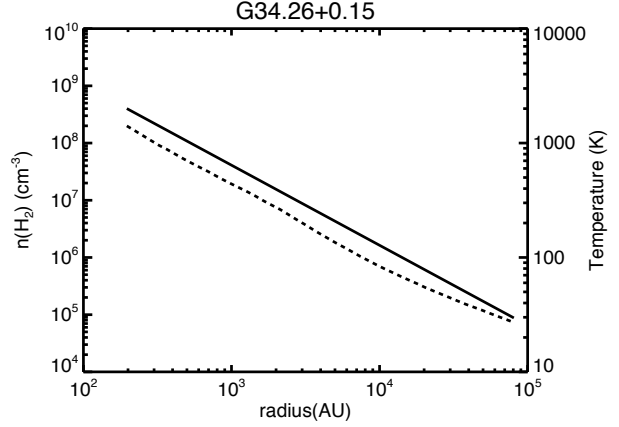


**Figure B1.**  $\text{H}_2$  density (solid line) and temperature (dashed line) profiles from van der Tak et al. (2013).

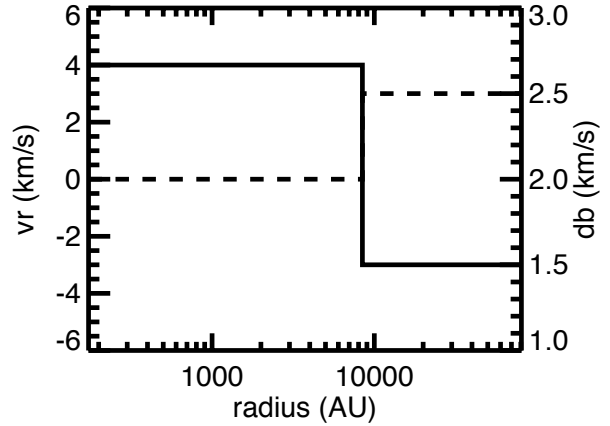


**Figure B2.** Radial velocity ( $v_r$ , solid line) and Doppler b-parameter ( $db$ , dashed line) profiles assumed for the different models presented in the paper.

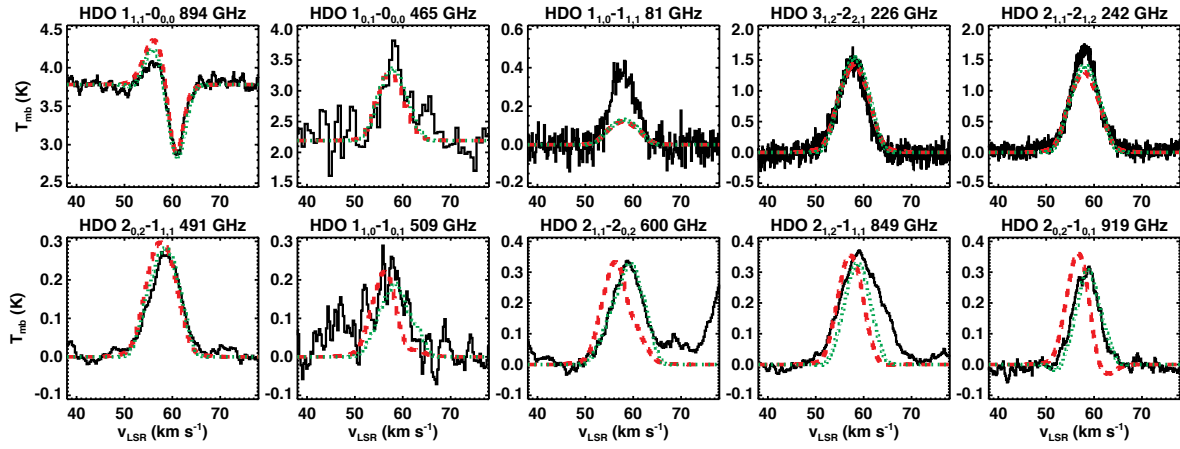
of the abundance between 100 and 200 K (see Section 4.2.5), we also checked that a radial velocity increasing gradually from  $-3$  to  $4 \text{ km s}^{-1}$  between 100 and 200 K would give similar results.

**B3 Modeling of the HDO lines with a two-jump modeling**

In their study of Sgr B2(M), Comito et al. (2010) showed that a model with two abundance jumps, one at 100 K and another at 200 K, is necessary to reproduce the different HDO lines observed towards this star-forming region. To check the influence on our results, we ran grids with such assumptions for our modeling of G34. Several models give a good agreement with the data. However the fit to the data is not better than with one jump. It is extremely similar to the model shown in Figure 5. Unsurprisingly, the best-fit gives an inner abundance ( $T > 200 \text{ K}$ ) of  $2 \times 10^{-7}$ , consistent with a modeling with a unique jump at a temperature of 200 K. The outer abundance ( $T < 100 \text{ K}$ ) is estimated to be  $8 \times 10^{-11}$ , and the abundance between 100 and 200 K is only constrained by an upper limit of  $1 \times 10^{-9}$ . Indeed, with abundances higher than  $1 \times 10^{-9}$ , the predicted intensities for the lines at 491, 600 and 919 GHz become too high compared with the observations. These results are consis-

**Table A1.** List of the *Herschel*/HIFI obsIDs

Species	Frequency (GHz)	Transition	ObsID-A	ObsID-B	ObsID-C	Observing program
HDO	490.5966	2 <sub>0,2</sub> –1 <sub>1,1</sub>	1342244320	1342244321	1342244322	OT1
HDO	509.2924	1 <sub>1,0</sub> –1 <sub>0,1</sub>	1342219186	1342219187	1342219188	PRISMAS
HDO	599.9267	2 <sub>1,1</sub> –2 <sub>0,2</sub>	1342230375	1342230376	1342230377	OT1
HDO	848.9618	2 <sub>1,2</sub> –1 <sub>1,1</sub>	1342244114	1342244115	1342244116	OT1
HDO	893.6387	1 <sub>1,1</sub> –0 <sub>0,0</sub>	1342207360	1342207361	1342207362	PRISMAS
HDO	919.3109	2 <sub>0,2</sub> –1 <sub>0,1</sub>	1342244381	1342244382	1342244383	OT1
ortho-H <sub>2</sub> <sup>18</sup> O	547.6764	1 <sub>1,0</sub> –1 <sub>0,1</sub>	1342194468	1342194469	1342194470	PRISMAS
para-H <sub>2</sub> <sup>18</sup> O	1101.6983	1 <sub>1,1</sub> –0 <sub>0,0</sub>	1342207367	1342207368	1342207369	PRISMAS


**Figure B3.** Black solid line: HDO lines observed with HIFI, IRAM, and CSO. Red dashed line: Modeling with an infall profile (free-fall model with  $M = 20 M_{\odot}$ ). Green dotted line: Modeling with a velocity profile with inward motions in the outer regions and outward motions in the inner regions.

tent with a modeling having a single jump, and the two-jump assumption does not improve the fit of the model results to the data. Although we cannot exclude that a double abundance jump occurs here, we estimate that the hypothesis of one jump is probably more reasonable. Indeed, chemical reasons for a three-step abundance profile are unclear. All the HDO trapped in the grain mantles should desorb thermally at approximately 100 K. Additional formation of water is possible into the gas phase at higher temperatures. But due to the relatively high temperatures in the hot core, the formation of deuterated water should be negligible. In addition, the HDO abundances derived between 100 and 200 K are very low ( $\leq 1 \times 10^{-9}$ ) comparatively to the abundance above 200 K ( $\sim 2 \times 10^{-7}$ ). Uncertainty in the temperature profile in the inner region with a single jump produced by the desorption from grain mantles or a gradual increase of the abundance probably provide a better explanation than a two jump model.

#### B4 Summary of the different models

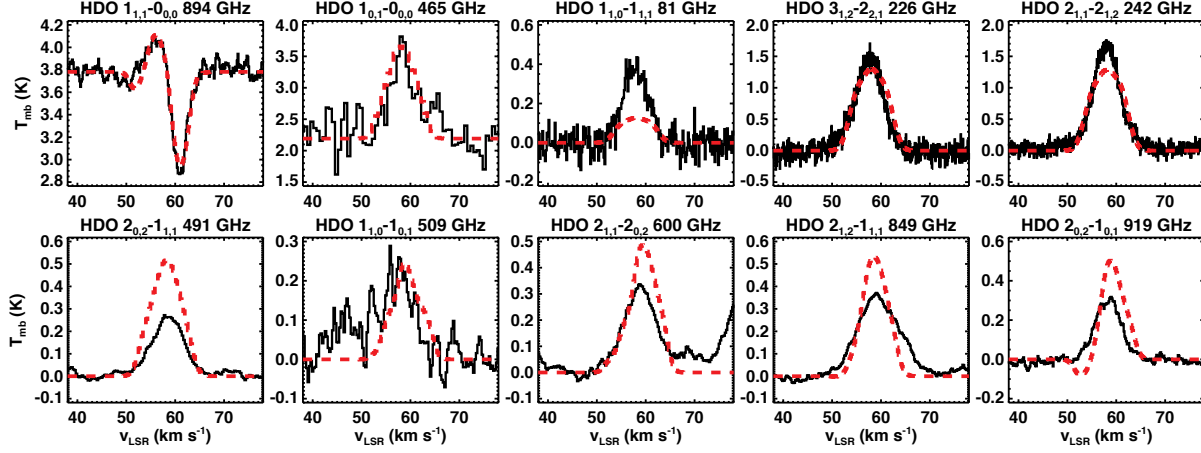
Table B1 summarizes the different types of models shown in the paper.

#### APPENDIX C: SENSITIVITY OF OUR MODELING TO THE INCLUSION OF SPIN-STATE CHEMISTRY

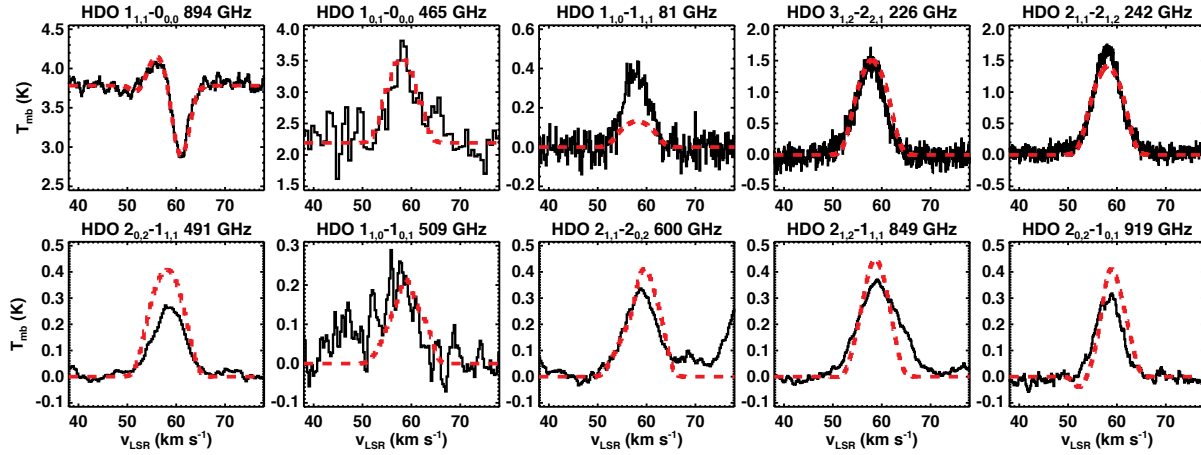
We studied the sensitivity of our results to the chemistry involving the spin states of H<sub>2</sub>, D<sub>2</sub>, H<sub>3</sub><sup>+</sup>, H<sub>2</sub>D<sup>+</sup>, D<sub>2</sub>H<sup>+</sup>, and D<sub>3</sub><sup>+</sup>. Using the same physical condition as described in section 5.1, we modeled the chemical evolution of our source using our basic chemical network adapted from Aikawa et al. (2012) and Furuya et al. (2012), without taking into account spin states. Figure C1 presents calculated gaseous HDO and H<sub>2</sub>O abundances, and HDO/H<sub>2</sub>O ratios, with and without spin-state chemistry.

The gaseous HDO abundance is higher throughout the source by a factor 2 (inner core) to 4 (cold envelope), if we neglect spin state chemistry. We expected this result since the inclusion of spin states tends to reduce deuterium fractionation by populating ortho spin states of H<sub>2</sub>. The effect is more pronounced in the cold envelope because the endothermic reactions involving deuterated ions and o-H<sub>2</sub> are greatly enhanced in rate. The differences are time dependent, and are less pronounced as the system progresses from the IRDC phase to the end of the simulation because o-H<sub>2</sub> is converted in p-H<sub>2</sub>.

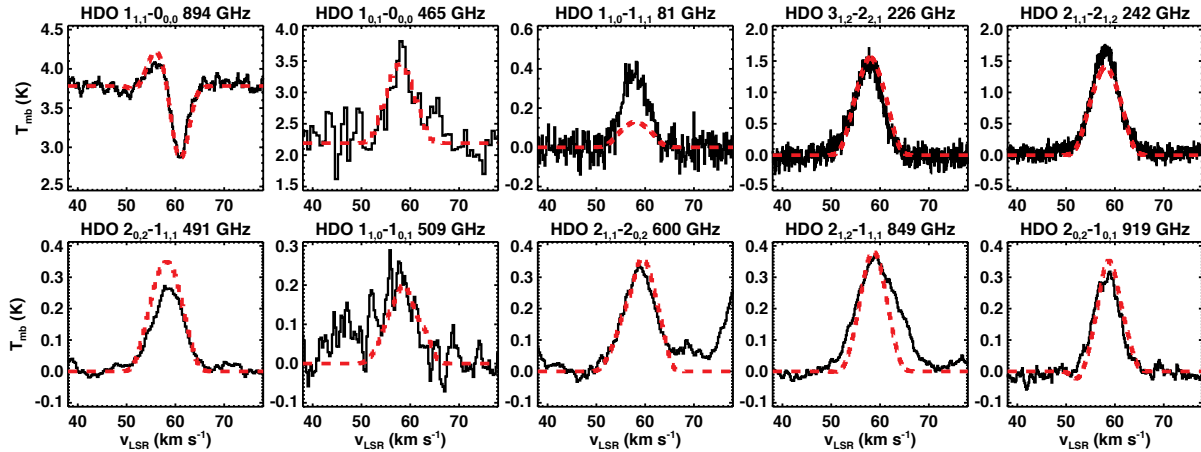
In the hot inner region ( $\leq 10^4$  AU) both models give the same results for gas-phase water. In the cold envelope, there is more gas phase water if we take into account spin-state chemistry. Contrary to HDO, the differences grow larger with time, and this trend is par-



**Figure B4.** Black solid line: HDO lines observed with HIFI, IRAM, and CSO. Red dashed line: Modeling for a jump temperature  $T_j = 120$  K, an inner abundance  $X_{\text{in}} = 6 \times 10^{-8}$  and an outer abundance  $X_{\text{out}} = 8 \times 10^{-11}$ .



**Figure B5.** Black solid line: HDO lines observed with HIFI, IRAM, and CSO. Red dashed line: Modeling for a jump temperature  $T_j = 150$  K, an inner abundance  $X_{\text{in}} = 1 \times 10^{-7}$  and an outer abundance  $X_{\text{out}} = 8 \times 10^{-11}$ .

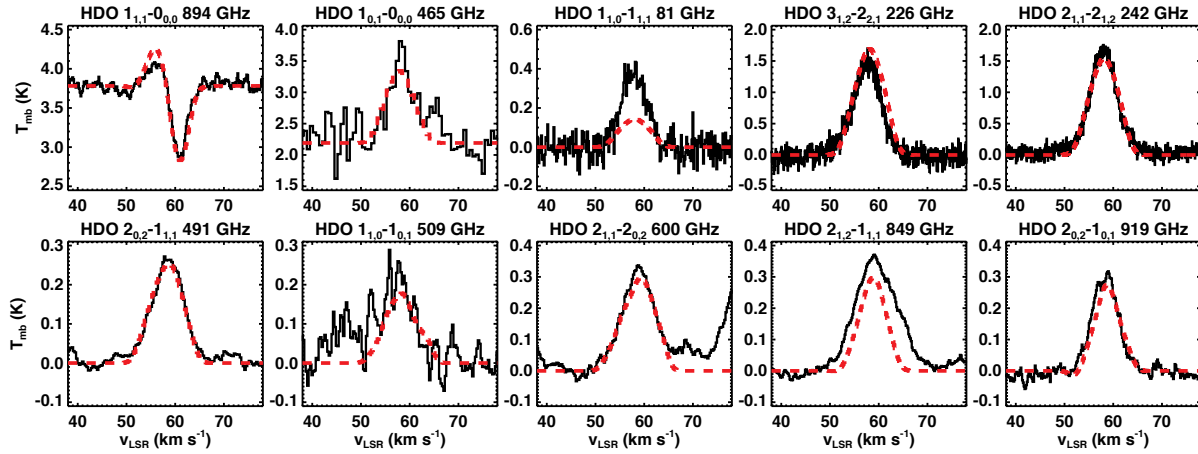
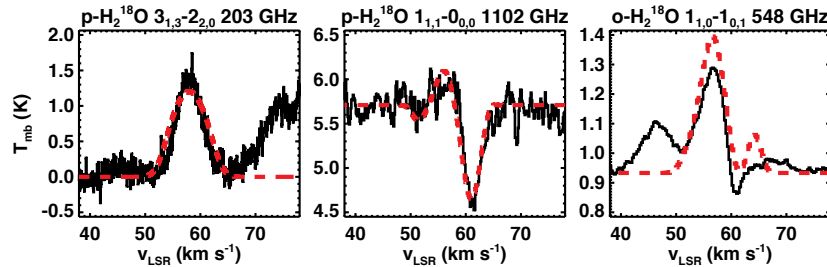


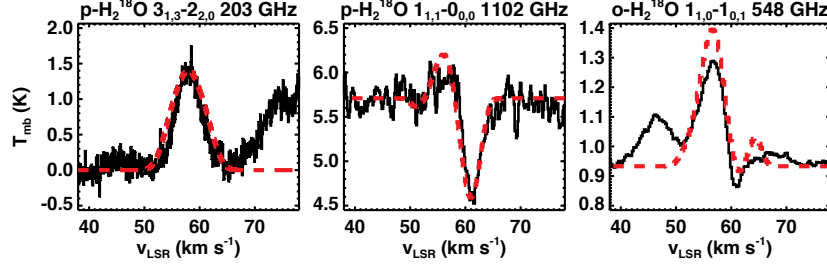
**Figure B6.** Black solid line: HDO lines observed with HIFI, IRAM, and CSO. Red dashed line: Modeling for a jump temperature  $T_j = 180$  K, an inner abundance  $X_{\text{in}} = 1.5 \times 10^{-7}$  and an outer abundance  $X_{\text{out}} = 8 \times 10^{-11}$ .



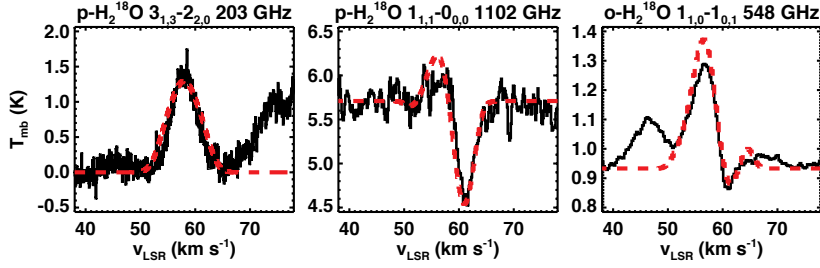
**Table B1.** List of the models presented in the paper.

Model	Abundance profile	Sections & Figures
1	1 jump $T_j = 100$ K	HDO : Sect. 4.2.2, Fig. 4
2	1 jump $T_j = 120$ K	HDO : Sect. 4.2.2, Fig. B4
3	1 jump $T_j = 150$ K	HDO : Sect. 4.2.2, Fig. B5 $\text{H}_2^{18}\text{O}$ : Sect. 4.2.3, Fig. B8
4	1 jump $T_j = 180$ K	HDO : Sect. 4.2.2, Fig. B6 $\text{H}_2^{18}\text{O}$ : Sect. 4.2.3, Fig. B9
5	1 jump $T_j = 200$ K	HDO : Sect. 4.2.2, Fig. 5 $\text{H}_2^{18}\text{O}$ : Sect. 4.2.3, Fig. 6
5	1 jump $T_j = 220$ K	HDO : Sect. 4.2.2, Fig. B7 $\text{H}_2^{18}\text{O}$ : Sect. 4.2.3, Fig. B10
6	2 jumps $T_{j1} = 100$ K, $T_{j2} = 200$ K	HDO : Appx. B3
7	Constant inner abundance ( $T \geq 200$ K) and decrease of the outer abundance from the cold to the warm regions (see Fig. 7)	HDO : Sect. 4.2.4, Fig. 8 $\text{H}_2^{18}\text{O}$ : Sect. 4.2.4, Fig. 9
8	Constant inner abundance, gradual increase of the abundance at the transition hot core/cold envelope (100–200 K) and decrease of the outer abundance from the cold regions to the regions at 100 K (see Fig. 7)	HDO : Sect. 4.2.5, Fig. 8 $\text{H}_2^{18}\text{O}$ : Sect. 4.2.5, Fig. 9


**Figure B7.** Black solid line: HDO lines observed with HIFI, IRAM, and CSO. Red dashed line: Modeling for a jump temperature  $T_j = 220$  K, an inner abundance  $X_{\text{in}} = 3 \times 10^{-7}$  and an outer abundance  $X_{\text{out}} = 8 \times 10^{-11}$ .

**Figure B8.** Black solid line:  $\text{H}_2^{18}\text{O}$  lines observed with HIFI and IRAM. Red dashed line: Modeling for a jump temperature  $T_j = 150$  K, an inner abundance  $X_{\text{in}} = 4 \times 10^{-7}$  and an outer abundance  $X_{\text{out}} = 1.3 \times 10^{-10}$ .



**Figure B9.** Black solid line:  $\text{H}_2^{18}\text{O}$  lines observed with HIFI and IRAM. Red dashed line: Modeling for a jump temperature  $T_j = 180$  K, an inner abundance  $X_{\text{in}} = 7 \times 10^{-7}$  and an outer abundance  $X_{\text{out}} = 1.3 \times 10^{-10}$ .



**Figure B10.** Black solid line:  $\text{H}_2^{18}\text{O}$  lines observed with HIFI and IRAM. Red dashed line: Modeling for a jump temperature  $T_j = 220$  K, an inner abundance  $X_{\text{in}} = 1.2 \times 10^{-6}$  and an outer abundance  $X_{\text{out}} = 1.3 \times 10^{-10}$ .

ticularly strong in the transition area ( $\approx 10^4$  AU). In this area, the temperature is low enough to not allow efficient desorption, and the density is high so adsorption is important. In consequence, water is primarily on the grain surfaces. In this situation, gas phase reactions are the principal pathway to form gas phase water, mainly through  $\text{H}_3\text{O}^+$ : the spin-state chemistry reduces the formation of  $\text{H}_2\text{D}^+$  from  $\text{H}_3^+$ , and the extra amount of  $\text{H}_3^+$  helps to produce more  $\text{H}_3\text{O}^+$  through successive reactions involving OH,  $\text{H}_2\text{O}^+$ , and  $\text{H}_2$ .

Globally, since the HDO abundance is lower and the  $\text{H}_2\text{O}$  abundance is higher if we take into account spin-state chemistry, the HDO/ $\text{H}_2\text{O}$  ratio is lower. The decrease is within a factor of 10, and depends on the radius and the time. The differences are less critical at high temperature than at low temperature, but are not negligible compared with the variation of our measured ratios.

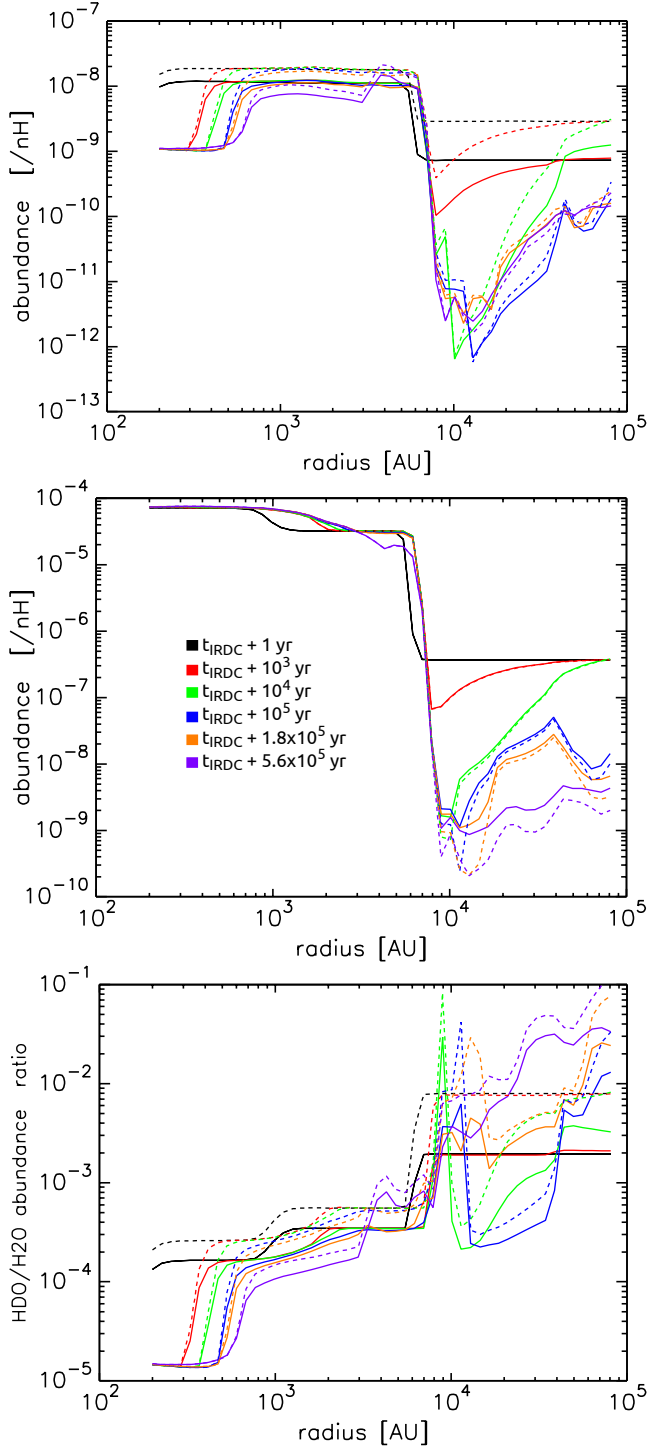


**Figure C1.** Calculated gas-phase abundances of HDO (top panel) and H<sub>2</sub>O (middle panel) vs radius with (solid lines) and without (dashed lines) spin-state chemistry. The bottom panel shows the corresponding HDO/H<sub>2</sub>O ratios. The results are time dependent, and the colors correspond to different values after the first initial phase as in figure 10.